How bias correction goes wrong: Measurement of X_{CO_2} affected by erroneous surface pressure estimates

Matthäus Kiel[1], Christopher W. O'Dell[4], Brendan Fisher[3], Annmarie Eldering[3], Ray Nassar[5], Cameron G. MacDonald[6], and Paul O. Wennberg[1,2]

[1]Division of Geological and Planetary Sciences, California Institute of Technology, Pasadena, CA, USA
[2]Division of Engineering and Applied Sciences, California Institute of Technology, Pasadena, CA, USA
[3]Jet Propulsion Laboratory, California Institute of Technology, Pasadena, CA, USA
[4]Colorado State University, Fort Collins, CO, USA
[5]Climate Research Division, Environment and Climate Change Canada, Toronto, ON, Canada
[6]Department of Physics and Astronomy, University of Waterloo, Waterloo, ON, Canada

Correspondence: Matthäus Kiel (mkiel@caltech.edu)

Abstract. Currently all measurements of X_{CO_2} from space have systematic errors. To reduce a large fraction of these errors, a bias correction is applied to X_{CO_2} retrieved from GOSAT and OCO-2 spectra using the ACOS retrieval algorithm. The bias correction uses, among other parameters, the surface pressure difference between the retrieval and the meteorological reanalysis. Relative errors in the surface pressure estimates, however, propagate nearly 1:1 into relative error in bias-corrected X_{CO_2}. For OCO-2, small errors in the knowledge of the pointing of the observatory (up to $\sim$130 arcsec) introduce a bias in X_{CO_2} in regions with rough topography. Erroneous surface pressure estimates are also caused by an coding error in ACOS version 8, sampling meteorological analyses at wrong times (up to three hours after the overpass time). Here, we derive new geolocations for OCO-2's eight footprints and show how using improved knowledge of surface pressure estimates in the bias correction reduces errors in OCO-2's v9 X_{CO_2} data.

1 Introduction

Atmospheric carbon dioxide (CO_2) is currently being measured from space by, among other instruments, NASA's Orbiting Carbon Observatory 2 (OCO-2) and JAXA's Greenhouse gases Observing SATellite (GOSAT). Accurate and precise measurements of atmospheric CO_2 can identify and quantify its sources and sinks and, more generally, improve our understanding of biosphere-atmosphere fluxes. To do so, these measurements must be sufficiently accurate and precise to properly capture the small ($<1\%$) spatial and temporal gradients of CO_2. OCO-2 and GOSAT X_{CO_2} data have been widely used in studies to characterize fluxes from different sources, e.g. emissions from power plants (Nassar et al., 2017) or fires in Indonesia (Heymann et al., 2017). Other recent studies analyzed flux anomalies during El Niño periods (Liu et al., 2017).

OCO-2 and GOSAT share a common observational approach: solar reflectance spectra centered around 1.6 µm and 2.0 µm are used to determine the CO_2 optical depth. The O_2 optical depth is observed at the so-called 'A-band' centered around 0.76 µm. The column-averaged dry air mole fraction of CO_2 (X_{CO_2}) is determined by combining the information from these three spectral regions. The A-band is used to determine the amount of dry air along the O_2 optical path from the sun to the

spectrometer (airmass). The two CO_2 bands provide a measure of how many CO_2 molecules are in the (nearly) similar path. X_{CO_2} is the ratio of CO_2 to the dry surface pressure. Any error that does not affect both, the CO_2 measurement and dry surface pressure, in the same way, is expected to propagate into X_{CO_2}. A fundamental challenge for the retrieval is that photons are scattered in the atmosphere and the efficiency of the scattering – primarily by clouds and aerosols – depends on wavelength. The wavelength dependent scattering is, in turn, estimated by the retrieval algorithm using information from both the O_2 spectra and the relative CO_2 optical depths determined from the two different CO_2 bands.

Early analysis of X_{CO_2} from the initial GOSAT spectra had global and regional systematic errors. Wunch et al. (2011b) demonstrated, however, that a large fraction of the error in X_{CO_2} was correlated with retrieved components of the state vector in the retrieval algorithm. In particular, difference between the retrieval of surface pressure and that from the meteorological reanalysis was shown to correlate with error of similar magnitude in X_{CO_2} (e.g. when the surface pressure retrieval was $\sim$1% too large, the retrieved X_{CO_2} was $\sim$1% too small). There are several reasons why surface pressure is not accurately retrieved from the spectra. First, errors in the knowledge of the spectroscopy of the oxygen can produce spurious airmass dependencies and can affect the pressure retrieval (e.g. Yang et al., 2005; Wunch et al., 2011a). Second, the algorithm is not adequately able to distinguish pathlength errors due to scattering from those due to surface pressure variation. For example, overestimates of the amount of aerosol near the surface (which shortens the path) can be compensated by an overestimate of surface pressure. Because in the retrieval aerosols are generally assumed to scatter less efficiently at longer wavelengths, error in retrieved pathlength maps differently into O_2 and CO_2, resulting in a bias in X_{CO_2}. Pathlength errors also largely depend on surface albedo. For example, if the surface albedo is high, multiple reflections between the surface and the aerosol layer are efficient and lengthen the path. Moreover, the spectral variation of surface albedo and aerosol optical properties also change the radiative transfer between the A-band and CO_2 bands. For example, differences in the absorption optical thickness structure between the three bands induce band dependent height sensitivities to different types of aerosols in the retrieval.

Several retrieval codes that have been used to analyze GOSAT and OCO-2 spectra treat this problem differently. For example, the RemoTeC algorithm does not retrieve the surface pressure from the spectra. It uses the surface pressure from the meteorological reanalysis (Butz et al., 2011; Wu et al., 2018). Others, such as the University of Leicester Full Physics algorithm (UoL-FP) first normalizes the retrieved X_{CO_2} by the ratio of the retrieved surface pressure from the spectra and the surface pressure from the meteorological reanalysis. Then it uses the difference between the retrieved surface pressure and that from the meteorological reanalysis to 'bias correct' the X_{CO_2} product (Cogan et al., 2012). To date, all versions of the Atmospheric Carbon Observations from Space (ACOS) retrieval algorithm (O'Dell et al., 2012; Crisp et al., 2012; O'Dell et al., 2018), used for both OCO-2 and GOSAT spectra, also have used the surface pressure difference between the retrieval and that diagnosed from the meteorological reanalysis to bias correct the X_{CO_2} product. This bias correction demonstrably improves the data set (Wunch et al., 2011b, 2017b; O'Dell et al., 2018). It also, however, places new demands on the accuracy of the meteorological analysis – demands that had not been considered at the time the OCO-2 mission was conceived. Error in the assumed pressure from the meteorological reanalyses at the field of view of the spectrometers will propagate nearly 1:1 into bias-corrected X_{CO_2}. Over land, for example, small errors in the knowledge of the pointing of the observatory can yield significant errors in estimates of surface pressure in regions with rough topography. This is illustrated in Wunch et al. (2017b) where X_{CO_2} variations

near Lauder, New Zealand showed strong sensitivity to (different) estimates of the pointing of OCO-2, introducing an apparent topography related bias in the data. Finally, due to atmospheric tides, the estimate of the surface pressure is sensitive to when the meteorological reanalysis is sampled. Given the precision we need to achieve in X_{CO_2} measurements, seemly insignificant issues can not necessarily be ignored. For example, the mean canopy height of the Amazon rain forest is $\sim$25 m (Benson et al., 2016) and might vary temporally due to fires or deforestation. Furthermore, the usual tidal range in the open ocean is $\sim$0.5 m but coastal tidal ranges can reach up to 12 m (NOAA, last access: Aug. 2018). At sea level, altitude variations of $\sim$8 m correspond to changes in surface pressure of $\sim$1 hPa. This might introduce errors in X_{CO_2} in the order of $\sim$0.4 ppm.

In this analysis, we address two issues with the OCO-2 v8 estimate of surface pressure: erroneous surface pressure values from the meteorological reanalysis due to small miss-specifications of the geolocations of OCO-2's eight footprints in the instrument-to-spacecraft pointing offsets, and erroneous surface pressure estimates due to sampling the meteorological reanalysis at incorrect times. We illustrate how, using improved knowledge of the surface pressure, we can improve the bias correction and reduce errors in X_{CO_2}. The resulting hybrid product which uses v8 retrieval results with a revised bias correction using updated surface pressure estimates is labeled as version 9 (v9). This paper is structured as follows: section 2 describes the impact of erroneous surface pressure estimates in the bias correction on X_{CO_2} estimates. New footprint geolocations for OCO-2 are derived in section 3. Section 4 introduces the revised parametric bias correction in v9 and discusses changes in the v9 filtration scheme. Section 5 gives a brief evaluation of the OCO-2 v9 data product and illustrates changes and improvements of v9 over v8 X_{CO_2} on regional and global scales.

2 Biases in OCO-2 X_{CO_2} due to erroneous surface pressure estimates

OCO-2 v8 X_{CO_2} estimates are derived using the ACOS retrieval algorithm. The algorithm uses optimal estimation to solve for parameters of the state vector to obtain the best match to spectra recorded in OCO-2's three spectral bands. The state vector includes, among other parameters, the surface pressure which is primarily derived from information retrieved from the O_2 A-band (but substantially constrained by the surface pressure prior). The prior surface pressure is taken from the GEOS-5 Forward Processing for Instrument Teams Atmospheric Data Assimilation System (GEOS5-FP-IT; Suarez et al., 2008; Lucchesi, 2013) and is sampled at the geolocation of each OCO-2 sounding. Surface pressure and prior surface pressure are used in the bias correction of X_{CO_2}. The OCO-2 bias correction addresses three types of biases: footprint dependent biases, parameter dependent biases, and a global scaling of X_{CO_2} to the World Meteorological Organization (WMO) trace-gas standard scale using comparisons to the Total Carbon Column Observing Network (TCCON; Wunch et al., 2011a). An overview of the three different bias correction terms is given in Mandrake et al. (2015), Wunch et al. (2017b), and O'Dell et al. (2018).

Biases in OCO-2 X_{CO_2} due to erroneous surface pressure estimates were initially illustrated in OCO-2 observations over Lauder, New Zealand (Fig. 10 in Wunch et al., 2017b). The Lauder TCCON site is situated in a remote area with no urban sources of X_{CO_2} nearby (Pollard et al., 2017). The area is dominated by rolling hills with mountain ridges spanning from southwest to northeast, almost perpendicular to the ground-track of the observatory (southeast to northwest). The terrain changes up to $\pm$200 m in altitude over small distances (see Fig. 2, upper panel). The middle panel of Fig. 2 shows X_{CO_2} enhancements

retrieved by the ACOS algorithm (version 8) over Lauder for a target observation on February 17, 2015. No bias correction is applied here. X_{CO_2} estimates are uniformly distributed over the observed scene with a mean value of 393.58 ppm and a standard deviation of 0.92 ppm. The lower panel of Fig. 2 shows OCO-2 X_{CO_2} estimates after the v8 bias correction is applied. The bias correction changes the mean value to 395.95 ppm and increases the standard deviation to 1.35 ppm. Bias corrected X_{CO_2} enhancements vary up to ± 3 ppm over the observed scene. The bias is spatially correlated with the underlying topography, more precisely, with the topographic slopes. The observed bias is introduced by erroneous values of the prior surface pressure in the dP term (the difference between the retrieved surface pressure and the prior surface pressure) in the parametric bias correction. The parametric bias correction accounts for spurious variability in X_{CO_2} which correlates with retrieval parameters like albedo, retrieval aerosol quantities, or surface pressure. A multivariate regression is performed between spurious X_{CO_2} variability and the parameters that account for the largest variance in the data to correct for these errors (Wunch et al., 2011b; Mandrake et al., 2015; O'Dell et al., 2018). The erroneous values of the prior surface pressure are caused by small misspecifications in the geolocations of OCO-2's eight footprints in the specified instrument-to-spacecraft pointing. As stated previously, at sea level, a surface pressure difference of 1 hPa corresponds to an altitude difference of $\sim$8 m. Therefore, in areas like Lauder with steep topography, misspecifications in the pointing of the observatory of a few arcsec can cause the prior surface pressure to be substantially different from the retrieved surface pressure. This introduces errors in bias-corrected X_{CO_2}, typically observed on local scales in areas with highly varying topography.

Another source for erroneous surface pressure estimates in v8 is caused by a temporal sampling error of the surface pressure estimate from the meteorological reanalysis. The prior surface pressure is taken from the GEOS5-FP-IT three-hourly output. A coding error in the meteorological sampling algorithm caused for some soundings the surface pressure estimate to be sampled as much as three hours after the overpass time. This mostly affected soundings of orbits whose first and last sounding fully lies between synoptic GEOS5-FP-IT's three-hourly outputs (0z, 3z, etc); the soundings in such an orbit would be erroneously sampled at the upper bounding synoptic time for that orbit. For example, for an orbit whose soundings lie fully between 6:00 UTC and 9:00 UTC, the OCO-2 meteorological sampling algorithm erroneously samples the GEOS5-FP-IT surface pressure field at 9:00 UTC for each sounding in that orbit. On average, this introduced a mean prior surface pressure error of about +0.5 hPa for affected soundings. In some cases, however, the prior surface pressure error reached up to $\pm$ 20 hPa for individual soundings. The sampling error also affects temperature and water vapor. Soundings over land are affected more than over ocean since diurnal surface heating tends to be stronger over land and because the surface pressure bias correction term over land is nearly 50% larger than over water. While the sampling error of the prior surface pressure is easy to correct for via the bias correction by fixing the coding error and re-running the meteorological sampling algorithm, erroneous surface pressure estimates caused by misspecifications in the instrument pointing offsets need greater attention.

3 Evaluation of OCO-2's footprint geolocations

The core of the OCO-2 instrument is a three-channel grating spectrometer that records spectra of reflected sunlight in the O_2 A-band (0.76 $\mu\mathrm{m}$), the weak CO_2 band (1.61 $\mu\mathrm{m}$), and the strong CO_2 band (2.06 $\mu\mathrm{m}$). The incoming light is guided through

a common optics assembly but the light is sampled and focused sequentially and independently onto three spectrometer slits, each 3 mm long and 28 $\mu\mathrm{m}$ wide (Haring et al., 2004; Crisp et al., 2017). These long, narrow slits are aligned to produce nominally co-boresighted fields of view. After passing the slit and being spectrally dispersed, the light is focused on a two dimensional focal plane array (FPA) with eight independent readouts along the slits - the so called footprints. Spectra for the three spectral bands and each footprint are recorded simultaneously.

To obtain the best estimate for the geolocation of the eight footprints, the following must be known: 1) the location of the spacecraft along the orbit track, 2) the pointing of the instrument boresight relative to a local coordinate system, and 3) the relative pointing of the fields of view (FOV) of the eight footprints in the three spectrometers. A Global Positioning System (GPS) sensor provides the location of the observatory along its orbit track. The on-board star tracker determines the orientation of the observatory relative to fixed stars. The relative alignment of the eight footprints is characterized with respect to the spacecraft body axes. The spatial FOV, defined along the long axis of the slit by the eight footprints, is aligned parallel with the spacecraft y-axis. The boresight of the spectrometer points down the -x-axis. The spacecraft z-axis points across the narrow axis of the spectrometer slit, perpendicular to the y-axis (see Fig. 1). For nadir and glint measurements, the z-axis is rotated around the -x-axis so it is oriented 30° (clockwise from above) from the principal plane (i.e. the plane that includes the sun, the surface target and the instrument aperture). To maintain this viewing geometry, the spacecraft slowly rotates counter clockwise (from above) around the -x-axis as it travels from the southern terminator, across the sub-solar latitude, to the northern terminator. South of a latitude that is $\sim 30°$ north of the sub-solar latitude, footprint 1 (FP 1) is to the west of footprint 8 (FP 8). North of this latitude, FP 1 is east of FP 8. For target mode observations, the z-axis is always pointed along the spacecraft orbit track, so that FP 1 is always to the west of FP 8. Pre-launch instrument ground-tests were performed to characterize the spatial FOV of each footprint and correction factors - the so called pointing offsets - have been derived and integrated into the geometric calibration algorithm (v0001 configuration, see Fig. 3). The pointing offsets are in the order of hundreds of arcsec. A change in the pointing offsets of, for example, 25 arcsec corresponds to a shift of the instrument FOV of $\sim$80 m at nadir. During the OCO-2 in-orbit checkout (IOC) period in 2014, lunar measurements were performed and in combination with data from coastal crossings the alignment of the three spectrometer slits was tested. The alignment of the instrument angular footprints in the coordinate system defined by the star tracker was within mission requirements (< 720 arcsec). Updated pointing offsets have been integrated into the geometric calibration algorithm in November 2014 (v0006 configuration, see Fig. 3). The findings in the previous section, however, indicate that a reevaluation of the pointing vector correction factors is desirable.

3.1 Methodology

The analysis of the IOC lunar data exposed some deficiencies of its usage in elaborating footprint geolocations: lunar data is typically taken in so-called single pixel mode (when each pixel of the array is read out individually; this is in contrast to normal operations where 20 spatial pixel samples are co-added to form each footprint), the moon only illuminates a fraction of the FPA, defocus compromises the analysis of the strong CO_2 band results, and the moon only provides positive constraints for the z-axis. To overcome the aforementioned limitations for the v0006 configuration, the IOC lunar data results were used to constrain the pointing vector for FP 6 and 7, whereas for the other FPs the ground-test results were used. Here, we follow a

different approach to derive new pointing offsets. We shift from estimating geolocations with lunar images, which are strictly geometric measurements, to optimizing footprint geolocations with retrieval variables. We utilize the ACOS Level 2 Full Physics (L2FP) algorithm and its associated pre-screeners, the A-band Preprocessor (ABP) and the IMAP-DOAS Preprocessor (IDP) to estimate footprint geolocations. The ABP performs a fast retrieval of surface pressure using the O_2 A-band and assumes that no clouds or aerosols are present. The IDP performs clear-sky fits to the weak and strong CO_2 bands to derive CO_2 columns (Taylor et al., 2016). Using the preprocessors over the L2FP algorithm saves computational effort and allows us to study pointing offsets for each spectral band individually. The footprint geolocations for the O_2 A-band are derived by minimizing the variation in the difference between the surface pressure retrieved from the ABP and the meteorological analysis ($\mathrm{dP_{ABP}}$). The location of the CO_2 band footprints is determined by minimizing the variation in the CO_2 columns divided by the dry air column determined from the meteorological analysis ($\mathrm{X_{CO_2,met}}$). These two metrics are systematically explored for a set of different pointing offsets. The geolocations that provide the smallest standard deviation over a given scene for $\mathrm{dP_{ABP}}$ are good estimates for the location of the O_2 A-band. The same holds for the standard deviation of $\mathrm{X_{CO_2,met}}$ regarding the weak and strong CO_2 band. The assumption here is that there are no significant variations in $\mathrm{X_{CO_2}}$ over the field of analysis. This may not be true in regions with large heterogeneous sources (e.g. urban areas) or sinks (vegetated areas) of CO_2 . It is only true for areas with a clean $\mathrm{X_{CO_2}}$ background. Therefore, in our analysis we focus on remote desert-like mountainous areas to study pointing offsets.

3.2 Training Dataset

We identify two desert areas in the northern and southern hemisphere with topographic relief and frequent clear sky conditions during nadir and glint observations to derive new footprint geolocations: a remote area in the Death Valley National Park, CA, USA, and an area in the Atacama Desert, Chile. The Death Valley National Park area ranges from 35° to 37°N and from 118° to 115°W. The area in the Atacama Desert ranges from 18° to 19°S and from 69.8° to 69.25°W. Both areas are far from anthropogenic CO_2 sources. A topography related bias in v8 $\mathrm{X_{CO_2}}$ is apparent in both areas (see Fig. 4). Observations over the Death Valley National Park include ∼1.800 soundings from September 2014 to September 2017. Observations over the Atacama Desert include ∼1.000 soundings from September 2014 to October 2017. All these soundings are aggregated into $0.02^\circ \times 0.02^\circ$ latitude-longitude grids. To account for the secular increase and seasonal cycle in CO_2 and different airmass values for different overpasses for each orbit, we normalize all $\mathrm{X_{CO_2,met}}$ soundings by the orbital mean. The orbital mean is calculated by taking into account all soundings of a particular orbit that are within the latitude and longitude limits of the analyzed scene. The standard deviation of $\mathrm{dP_{ABP}}$ and $\mathrm{X_{CO_2,met}}$ is calculated by taking into account all grid squares in the analyzed latitude and longitude limits. Analyzing data from both hemispheres allows us to check for possible errors introduced by the reversed orientation of the z- and y-axis in the northern and southern hemisphere in our pointing offset derivation (e.g. errors introduced by a timing error).

We run the ABP and IDP for a set of different pointing offsets for which the relative footprint positions of the v0006 configuration are preserved. If not otherwise stated, in the following we refer to the pointing offset of FP 4 of the O_2 A-band when we refer to pointing offset values. For example, if the pointing offset of FP 4 of the O_2 A-band is shifted by +25 arcsec

along the y-axis, then all other footprint geolocations are also shifted in the same direction by +25 arcsec along the y-axis (even though their absolute positions differ from the FP 4 O_2 A-band position). The same holds for the z-axis. For the y-axis, we run both algorithms for four different pointing offsets ranging from 175 to 250 arcsec in 25 arcsec steps. For each of these shifts, we also run a set of different offsets for the z-axis, ranging from -250 to +100 arcsec also in 25 arcsec steps. This leads to a total of 60 different geolocation configurations.

3.3 Results

Figure 5 shows the standard deviation of $\mathrm{dP_{ABP}}$ and $\mathrm{X_{CO_2,met}}$ for FP 4 for all 60 geolocation configurations for the Death Valley National Park. The observed metrics are less sensitive to changes along the footprint axis than along the z-axis. Differences in the standard deviation between neighboring pointing offsets are small, typically < 0.5 hPa for the O_2 A-band and < 0.2 ppm for the two CO_2 bands. This holds for all footprints in the three spectral bands. For example, for FP 2 to 7, the standard deviation of $\mathrm{dP_{ABP}}$ is minimized for a pointing offset of 225 arcsec along the footprint axis. A pointing offset of 200 arcsec minimizes the standard deviation of FP 1 and 8. Similar results are derived for the Atacama Desert (not shown here). In general, a pointing offset of 225 arcsec along the footprint axis minimizes the standard deviation of $\mathrm{dP_{ABP}}$ and $\mathrm{X_{CO_2,met}}$ for the majority of the footprints. This offset value is nearly identical to the v0006 configuration (222.4 arcsec). Therefore, we adapt a pointing offset of 225 arcsec along the y-axis for all footprints in the three spectral bands. The absolute pointing offsets along the footprint axis are summarized in Table 1.

Figure 6 shows the standard deviation of $\mathrm{dP_{ABP}}$ and $\mathrm{X_{CO_2,met}}$ as a function of the z-axis pointing offsets for FP 4 for the Death Valley National Park (for a pointing offset of 225 arcsec along the footprint axis). The analyzed metrics are strongly sensitive to changes of the pointing offset along this axis. We perform a quadratic regression to determine the best estimate of the location of the minimum. We only take data points into account that are distributed symmetrically around the minimum. For FP 4, our analysis indicates a minimum at -124 arcsec for the O_2 A-band, -71 arcsec for the weak CO_2 band, and -44 arcsec for the strong CO_2 band. We derive pointing offsets for all other footprints for all three bands in the same way. Figure 7 (upper panel) summarizes the z-axis pointing offsets for all footprints for all three bands for the Death Valley National Park and Atacama Desert. On average, the derived pointing offsets for the two areas differ by 13 arcsec for the weak CO_2 band and by 25 arcsec for the strong CO_2 band. For the O_2 A-band the differences between the two areas differ, on average, by 46 arcsec. Footprints 3 to 5 have the largest pointing offset values. This is in agreement with the relative footprint geolocations in the v0006 configuration. We average the derived pointing offsets for the CO_2 bands from both hemispheres. This provides the best estimate for the footprint geolocations globally and takes into account that the z-axis is rotated by nearly 180° (in glint and nadir mode) when the observatory overpasses the equator. However, for the O_2 A-Band, the difference between the pointing offsets for both areas reaches up to 60 arcsec for FP 2. In addition, the Atacama Desert analysis indicate larger relative pointing variations for neighboring footprints. Therefore, for the O_2 A-band, we only take the derived pointing offsets from the Death Valley National Park analysis into account. Final pointing offsets for all three bands are derived by applying a quadratic regression to the pointing offsets as a function of footprint. This preserves the parabolic shape of the relative footprint positions

which is supported by findings from the pre-launch and IOC lunar analysis. The updated pointing offsets for the z-axis for each spectral band are summarized in Table 1.

To evaluate the impact of the updated footprint geolocations we sample the surface pressure from GEOS5-FP-IT with the updated meteorological sampling algorithm (that was corrected for the time sampling error) at the footprint geolocations of the O_2 A-band. The surface pressure is mainly retrieved from the O_2 A-band, therefore sampling the meteorological reanalysis at the O_2 footprint geolocation should yield best surface pressure estimates. Figure 8 shows the prior surface pressure difference between v8 and sampled at the updated footprint geolocations. The striping pattern effect is mainly introduced by the updated sampling algorithm and follows orbital paths. As stated previously, the updated sampling method also introduces a mean bias of +0.5 hPa between the v8 and newly derived surface pressure estimates. Figure 9 shows the change between the standard deviation of the prior surface pressure in each grid box for both sampling methods. The observed structures are mainly driven by changes in the footprint geolocations. The largest changes are over mountainous regions, e.g. the Tibetan Plateau, the Andes, or the U.S. West Coast. This will mostly manifest as local scale changes in $\mathrm{X_{CO_2}}$. As expected, there are no significant changes over ocean due to the updated footprint geolocations.

4 The OCO-2 v9 data product

Our improved knowledge of OCO-2's footprint geolocations and the update of the meteorological sampling algorithm reduces errors in bias-corrected $\mathrm{X_{CO_2}}$ that were introduced through erroneous surface pressure estimates in the v8 bias correction. The OCO-2 v9 data product combines the v8 ACOS L2FP retrieval results with a revised bias correction using updated surface pressure estimates from GEOS5-FP-IT. Moreover, filter limits that define the $\mathrm{X_{CO_2}}$ quality flag and warn levels are adjusted leading to a larger number of soundings that pass the filtration. Finally, the global scaling factor that is derived from direct observations over TCCON stations is updated. This section highlights the major changes in OCO-2's v9 $\mathrm{X_{CO_2}}$. The techniques that are used in the next sections are those presented in O'Dell et al. (2018). The derived results, with exception of the revised parametric bias correction, represent updates of the findings in O'Dell et al. (2018).

4.1 Parametric Biases Correction

The parametric bias correction accounts for spurious variability in $\mathrm{X_{CO_2}}$ that is correlated with parameters in the retrieval state vector (Wunch et al., 2017b; O'Dell et al., 2018). A multivariate regression is performed between spurious $\mathrm{X_{CO_2}}$ variations and the parameters that account for the largest fraction of the spurious variability. For all ACOS versions for GOSAT and OCO-2 observations, the mode dependent parametric bias correction has the following form:

$$C_P = \sum_i c_i \left(p_i - p_{i,\mathrm{ref}}\right) \tag{1}$$

Here, c_i are regression coefficients, p_i are the selected parameters, and $p_{i,\mathrm{ref}}$ the corresponding reference values. To select the parameters and derive the regression coefficients, different truth proxy training data sets were used for v8: TCCON, Small Area Approximation (SAA), and Multi-Model Median. These truth proxies represent an independent estimate of $\mathrm{X_{CO_2}}$ to which we

compare OCO-2 X_{CO_2}. A detailed description of the truth proxies is given in Sect. 4.1 in O'Dell et al. (2018). For v8 land observations, three different parameters were identified that account for the largest fraction of variability: co2_grad_del, DWS, and dP. Over ocean, only co2_grad_del, and dP contribute to the parametric bias correction. co2_grad_del represents the tropospheric lapse rate of the retrieved CO_2 profile and is defined as the difference in the retrieved CO_2 between the surface and the retrieval pressure level at 0.6 times the surface pressure, minus the same quantity for the prior profile. DWS represents the combined retrieved optical depth of large particles in the lower-to-middle troposphere in the retrieval, namely dust, water cloud, and sea salt aerosol. In v8, dP is defined as the difference between the retrieved surface pressure and the prior surface pressure from GEOS5-FP-IT.

For v9, we define two different dP parameters for observations over land (dP_{frac}) and ocean (dP_{sCO_2}) that are used in the parametric bias correction. The revised dP parameters take into account two problems: 1) the misspecifications in the geolocation calibration algorithm for the overall pointing of the observatory and 2) the pointing offsets between the three spectral bands. The first is characterized by the difference between the retrieved surface pressure of the v8 L2FP algorithm ($P_{ret,v8}$) and the prior surface pressure at the new geolocation where the O_2 A-band is pointing (P_{ap,O_2}). The second is characterized by the difference between the prior surface pressure where the O_2 A-band is pointing and the prior surface pressure where the strong CO_2 band is pointing (P_{ap,sCO_2}). For ocean, the revised dP parameter has the following form (given in hPa):

$$\begin{aligned} dP_{sCO_2} &= (P_{ret,v8} - P_{ap,O_2}) + (P_{ap,O_2} - P_{ap,CO_2}) \\ &= P_{ret,v8} - P_{ap,sCO_2} \end{aligned} \tag{2}$$

This approach allows us to reduce variations in X_{CO_2} due to differences between the retrieved and estimated surface pressure without re-running the L2FP algorithm. Only the prior surface pressure sampled at the geolocation where the CO_2 bands are pointing is needed. Tests have shown that best results are achieved when the prior surface pressure is sampled at the geolocation of the strong CO_2 band. Over land, the revised dP parameter accounts for the fractional change in X_{CO_2} when error is present in surface pressure estimates (given in ppm):

$$dP_{frac} = X_{CO_{2,raw}} \left(1 - \frac{P_{ap,sCO_2}}{P_{ret,v8}}\right) \tag{3}$$

Here, $X_{CO_{2,raw}}$ represents the v8 X_{CO_2} from the L2FP run when no bias correction is applied. A theoretical motivation for our choice of the dP parameters over land and ocean is given in Appendix A. The definition of co2_grad_del and DWS remains the same in v9.

Similar to v8, we use three truth proxies to derive the parametric bias correction coefficients for co_grad_del, DWS and the revised dP parameters (see Table 2). Compared to v8, the truth proxy data sets are extended in time to cover the longer OCO-2 data record. For the Multi-Model Median, nine models from the OCO-2 model-intercomparison project (MIP) are used (see Table 3). For all datasets a correction was applied using the OCO-2 averaging kernels based on Connor et al. (2008). We convolve the CO_2 profiles from the truth proxies with the OCO-2 column averaging kernel before we compare it to OCO-2 X_{CO_2}. The parametric bias correction coefficients for v9 are derived from the average of all coefficients derived from the

different truth proxies. The adapted coefficients and reference values for land and ocean glint data are summarized in Table 4. The $\mathrm{dP_{frac}}$ coefficient over land is close to 1. This is in agreement with the theoretical value since a change in surface pressure by $\sim$1% changes $\mathrm{X_{CO_2}}$ by also $\sim$1% and seems to indicate that the retrieved surface pressure is still not sufficiently accurate to yield the best estimate of $\mathrm{X_{CO_2}}$; indeed, as shown in $\mathrm{X_{CO_2}}$, the coefficient implies that the optimal surface pressure is a weighted average of the retrieved and prior surface pressure, with the prior surface pressure weight being about 0.9. Figure 10 shows the different contributions of the v9 parametric bias correction to the raw $\mathrm{X_{CO_2}}$.

4.2 Quality Filters

Bad soundings (e.g. those affected by clouds, low continuum level signal-to-noise ratio, etc.) are mostly screened out by the ABP and IDP before the ACOS L2FP algorithm performs retrievals. Some soundings that pass the pre-screening criteria, however, show errors in raw $\mathrm{X_{CO_2}}$ when compared to the truth proxy training data sets that are too large to provide reliable constraints on $\mathrm{CO_2}$ fluxes. Therefore, threshold limits are defined for several variables to filter out these soundings. A detailed description on quality filtering is given Mandrake et al. (2015), Eldering et al. (2017), and O'Dell et al. (2018). We apply slight changes to the v9 filtration.

We introduce the new filter variables $\mathrm{dP_{O_2}}$ and $\mathrm{dP_{sCO_2}}$, the difference between the retrieved surface pressure and the estimated surface pressure at the geolocations of the $\mathrm{O_2}$ A-band and $\mathrm{dP_{sCO_2}}$ as given in Eq. (2). These variables replace the dP filter variable in v8, which was defined as the difference between the retrieved surface pressure and a mean surface pressure estimate at the geolocation of all three spectral bands. The improved knowledge of the estimated surface pressure values allows us to relax the filter limits for the standard deviation of the surface elevation in the FOV. Figure 9 shows the bias and scatter in $\mathrm{X_{CO_2}}$ over land relative to the Multi-Model Median truth proxy data set as a function of the standard deviation of the surface elevation. In v9, the scatter in the $\mathrm{X_{CO_2}}$ difference starts to increase for standard deviations of the surface elevation larger than $110\ \mathrm{m}$ whereas in v8 the scatter already increases for standard deviations larger than $60\ \mathrm{m}$. Therefore, we extend the rather strict upper filter limit of $60\ \mathrm{m}$ in v8 to $110\ \mathrm{m}$. This leads to a larger throughput of soundings in mountainous areas in v9. The parameters Max_Declocking_wco2 and Max_Declocking_sco2 are removed from the v9 filtration scheme over land. Moreover, filter limits for several other variables changed, e.g. rms_rel_wco2, τ_{oc}, Band 3 albedo, and $\mathrm{dP_{ABP}}$. The revised filter limits for rms_rel_wco2, τ_{oc}, and Band 3 albedo cause a larger throughput for regions with boreal forests at high northern latitudes. The updated limits for τ_{oc} and Band 3 albedo also increase the number of soundings over rain forests. The updated filter limits for $\mathrm{dP_{ABP}}$ cause a larger throughput in regions with bright surfaces, e.g. the Saharan desert (see Fig. 12). Overall, 10-15% additional soundings pass the new filtration scheme compared to v8. All v9 filter variables and limits for land and ocean observations are summarized in Table 5. For soundings that pass filtration in both v8 and v9, the quality flag did not change.

4.3 Global Scaling factor

The global scaling factor corrects for an overall bias in $\mathrm{X_{CO_2}}$ which still remains after filtration and application of the parametric bias correction. The global scaling factor is derived by comparing the OCO-2 data to TCCON measurements which

are tied to the WMO scale (e.g. Wunch et al., 2010; Messerschmidt et al., 2010; Geibel et al., 2012). Due to changes in the data filtration and the revised parametric bias correction in v9, the global scaling factor C_0 needs to be updated, too. TCCON stations that are used to derive the global scaling factor are listed in Table. 6.

We use the same geographic and temporal co-location criteria for OCO-2 data from direct overpasses of TCCON stations as in O'Dell et al. (2018). We apply the OCO-2 averaging kernels to TCCON data as discussed in the derivation of the coefficients in the parametric bias correction. The slope of the best fit line (forced through a zero intercept) is calculated using the method described in York et al. (2004). The global scaling factor is roughly the same for the different observational modes over land and ocean. Ultimately, we adapt a value of 0.9954 over land and 0.9953 over ocean in v9 (compared with 0.9958 over land and 0.9955 over ocean in v8).

5 Brief evaluation of OCO-2 $\mathbf{X_{CO_2}}$ data

Here, we evaluate the impact of the changes made in v9 on bias-corrected $\mathrm{X_{CO_2}}$. To explore changes on local scales, we revisit the target observation over Lauder, New Zealand on February 17, 2015. Figure 13 shows both v8 and v9 bias-corrected $\mathrm{X_{CO_2}}$. The improved knowledge of the prior surface pressure with the revised parametric bias correction clearly reduces the correlation between $\mathrm{X_{CO_2}}$ and the underlying topography in v9. $\mathrm{X_{CO_2}}$ values are distributed more uniformly over the observed scene. The standard deviation is reduced from 1.35 ppm in v8 to 0.74 ppm in v9. A small topography related bias is still apparent. However, compared to v8, it is a factor of two improvement in reducing biases caused by erroneous surface pressure estimates.

Figure 14 shows the absolute change in bias-corrected $\mathrm{X_{CO_2}}$ between v8 and v9 globally. The observed changes are mainly driven by three factors: the updated meteorological sampling algorithm, improved knowledge of the footprint geolocations, and the revised parametric bias correction. In analogy to Fig. 8, the striping patterns follow orbital paths and are caused by the updated meteorological sampling algorithm. Differences over mountainous regions like the Tibetan Plateau or the Andes are driven by the improved knowledge of the prior surface pressure due to the updated footprint geolocations. The revised $\mathrm{dP_{frac}}$ parameter in the parametric bias correction over land also introduces changes in regions at high altitudes but not necessarily with highly variable topography (e.g. South Africa). In addition, the v9 global scaling factor introduces a systematic difference of approximately +0.15 ppm between v8 and v9.

6 Conclusions

The update of the pointing vector that is used to derive the geolocation for OCO-2's eight footprints, together with an update of the meteorological sampling algorithm that corrects for a temporal sampling coding error, provides a better estimate for the surface pressure in OCO-2's v9 data product. Biases in $\mathrm{X_{CO_2}}$ due to erroneous surface pressure estimates are clearly reduced in regions with rough topography. For example, over Lauder, New Zealand, the standard deviation of bias-corrected $\mathrm{X_{CO_2}}$ is

reduced by almost a factor of two when the updated surface pressure estimates are used in the revised parametric bias correction that accounts for misspecifications in the instrument pointing offsets.

Accurate knowledge of the surface pressure and its estimate is crucial to retrieve $\mathrm{X_{CO_2}}$ accurately and many challenges remain. The OCO-2 retrieval, for example, still has a latitudinally-dependent bias in surface pressure with a maximum in the tropics of nearly 5 hPa (O'Dell et al., 2018). Currently, it is thought that this originates in errors in describing the temperature dependence of the oxygen absorption. Moreover, uncertainties in the underlying elevation map and the question what the source of the scattering is might have an impact on surface pressure estimates. This does not only affect $\mathrm{X_{CO_2}}$ retrieved from GOSAT and OCO-2 but may also affect future sensors with similar observational approaches.

Author contributions. MK performed substantial data analysis regarding the derivation of new pointing offsets, revised bias correction, and global scaling factor for v9. CO was involved in nearly all aspects of this work, in particular with the revised bias correction, quality filtering, and global scaling factor for v9. BF implemented many tests and performed data analysis. AE provided project leadership and algorithm guidance. CM and RN helped to understand the origin of the topography related bias and contributed to the selection of the training datasets. PW provided critical guidance on nearly all aspects of the work, throughout all stages.

Competing interests. The authors declare that they have no conflict of interest.

Acknowledgements. We thank David Crisp for helpful discussions on the viewing geometry of the observatory. We thank Callum McCracken for contributing to Fig. 4. This work was financially supported by NASA's OCO-2 project (grant no. NNN12AA01C), and NASA's carbon cycle and ecosystems research program (grant no. NNX17AE15G).

References

Baker, D. F., Bösch, H., Doney, S. C., O'Brien, D., and Schimel, D. S.: Carbon source/sink information provided by column CO_2 measurements from the Orbiting Carbon Observatory, Atmospheric Chemistry and Physics, 10, 4145–4165, https://doi.org/10.5194/acp-10-4145-2010, https://www.atmos-chem-phys.net/10/4145/2010/, 2010.

Basu, S., Guerlet, S., Butz, A., Houweling, S., Hasekamp, O., Aben, I., Krummel, P., Steele, P., Langenfelds, R., Torn, M., Biraud, S., Stephens, B., Andrews, A., and Worthy, D.: Global CO_2 fluxes estimated from GOSAT retrievals of total column CO_2, Atmospheric Chemistry and Physics, 13, 8695–8717, https://doi.org/10.5194/acp-13-8695-2013, https://www.atmos-chem-phys.net/13/8695/2013/, 2013.

Benson, M., Pierce, L., and Sarabandi, K.: Estimating boreal forest canopy height and above ground biomass using multi-modal remote sensing; a database driven approach, in: 2016 IEEE International Geoscience and Remote Sensing Symposium (IGARSS), pp. 2498–2501, 2016.

Blumenstock, T., Hase, F., Schneider, M., Garcia, O. E., and Sepulveda, E.: TCCON data from Izana (ES), Release GGG2014R0, TCCON data archive, hosted by CaltechDATA, https://doi.org/10.14291/tccon.ggg2014.izana01.R0/1149295, https://tccondata.org, 2014.

Butz, A., Guerlet, S., Hasekamp, O., Schepers, D., Galli, A., Aben, I., Frankenberg, C., Hartmann, J.-M., Tran, H., Kuze, A., Keppel-Aleks, G., Toon, G., Wunch, D., Wennberg, P., Deutscher, N., Griffith, D., Macatangay, R., Messerschmidt, J., Notholt, J., and Warneke, T.: Toward accurate CO2 and CH4 observations from GOSAT, Geophysical Research Letters, 38, https://doi.org/10.1029/2011GL047888, https://agupubs.onlinelibrary.wiley.com/doi/abs/10.1029/2011GL047888, 2011.

Chevallier, F., Ciais, P., Conway, T. J., Aalto, T., Anderson, B. E., Bousquet, P., Brunke, E. G., Ciattaglia, L., Esaki, Y., Fröhlich, M., Gomez, A., Gomez-Pelaez, A. J., Haszpra, L., Krummel, P. B., Langenfelds, R. L., Leuenberger, M., Machida, T., Maignan, F., Matsueda, H., Morguí, J. A., Mukai, H., Nakazawa, T., Peylin, P., Ramonet, M., Rivier, L., Sawa, Y., Schmidt, M., Steele, L. P., Vay, S. A., Vermeulen, A. T., Wofsy, S., and Worthy, D.: CO_2 surface fluxes at grid point scale estimated from a global 21 year reanalysis of atmospheric measurements, Journal of Geophysical Research: Atmospheres, 115, https://doi.org/10.1029/2010JD013887, https://agupubs.onlinelibrary.wiley.com/doi/abs/10.1029/2010JD013887, 2010.

Cogan, A. J., Boesch, H., Parker, R. J., Feng, L., Palmer, P. I., Blavier, J. L., Deutscher, N. M., Macatangay, R., Notholt, J., Roehl, C., Warneke, T., and Wunch, D.: Atmospheric carbon dioxide retrieved from the Greenhouse gases Observing SATellite (GOSAT): Comparison with ground-based TCCON observations and GEOS-Chem model calculations, Journal of Geophysical Research: Atmospheres (1984–2012), 117, https://doi.org/10.1029/2012JD018087, http:https://doi.org/10.1029/2012JD018087, 2012.

Connor, B. J., Boesch, H., Toon, G., Sen, B., Miller, C., and Crisp, D.: Orbiting Carbon Observatory: Inverse method and prospective error analysis, Journal of Geophysical Research: Atmospheres, 113, https://doi.org/10.1029/2006JD008336, https://agupubs.onlinelibrary.wiley.com/doi/abs/10.1029/2006JD008336, 2008.

Crisp, D., Fisher, B. M., O'Dell, C., Frankenberg, C., Basilio, R., Bösch, H., Brown, L. R., Castano, R., Connor, B., Deutscher, N. M., Eldering, A., Griffith, D., Gunson, M., Kuze, A., Mandrake, L., McDuffie, J., Messerschmidt, J., Miller, C. E., Morino, I., Natraj, V., Notholt, J., O'Brien, D. M., Oyafuso, F., Polonsky, I., Robinson, J., Salawitch, R., Sherlock, V., Smyth, M., Suto, H., Taylor, T. E., Thompson, D. R., Wennberg, P. O., Wunch, D., and Yung, Y. L.: The ACOS CO_2 retrieval algorithm - Part II: Global X_{CO_2} data characterization, Atmospheric Measurement Techniques, 5, 687–707, https://doi.org/10.5194/amt-5-687-2012, https://www.atmos-meas-tech.net/5/687/2012/, 2012.

Crisp, D., Pollock, H. R., Rosenberg, R., Chapsky, L., Lee, R. A. M., Oyafuso, F. A., Frankenberg, C., O'Dell, C. W., Bruegge, C. J., Doran, G. B., Eldering, A., Fisher, B. M., Fu, D., Gunson, M. R., Mandrake, L., Osterman, G. B., Schwandner, F. M., Sun, K., Taylor,

T. E., Wennberg, P. O., and Wunch, D.: The on-orbit performance of the Orbiting Carbon Observatory-2 (OCO-2) instrument and its radiometrically calibrated products, Atmospheric Measurement Techniques, 10, 59–81, https://doi.org/10.5194/amt-10-59-2017, https://www.atmos-meas-tech.net/10/59/2017/, 2017.

Crowell, S. M. R., Randolph Kawa, S., Browell, E. V., Hammerling, D. M., Moore, B., Schaefer, K., and Doney, S. C.: On the Ability of Space-Based Passive and Active Remote Sensing Observations of CO_2 to Detect Flux Perturbations to the Carbon Cycle, Journal of Geophysical Research: Atmospheres, 123, 1460–1477, https://doi.org/10.1002/2017JD027836, https://agupubs.onlinelibrary.wiley.com/doi/abs/10.1002/2017JD027836, 2018.

De Mazière, M., Sha, M. K., Desmet, F., Hermans, C., Scolas, F., Kumps, N., Metzger, J.-M., Duflot, V., and Cammas, J.-P.: TCCON data from Reunion Island (RE), Release GGG2014R0, TCCON data archive, hosted by CaltechDATA, https://doi.org/10.14291/tccon.ggg2014.reunion01.R0/1149288, https://tccondata.org, 2014.

Deutscher, N. M., Notholt, J., Messerschmidt, J., Weinzierl, C., Warneke, T., Petri, C., Grupe, P., and Katrynski, K.: TCCON data from Bialystok (PL), Release GGG2014R1, TCCON data archive, hosted by CaltechDATA, https://doi.org/10.14291/tccon.ggg2014.bialystok01.R1/1183984, https://tccondata.org, 2014.

Dubey, M., Henderson, B., Green, D., Butterfield, Z., Keppel-Aleks, G., Allen, N., Blavier, J.-F., Roehl, C., Wunch, D., and Lindenmaier, R.: TCCON data from Manaus (BR), Release GGG2014R0, TCCON data archive, hosted by CaltechDATA, https://doi.org/10.14291/tccon.ggg2014.manaus01.R0/1149274, https://tccondata.org, 2014.

Eldering, A., O'Dell, C. W., Wennberg, P. O., Crisp, D., Gunson, M. R., Viatte, C., Avis, C., Braverman, A., Castano, R., Chang, A., Chapsky, L., Cheng, C., Connor, B., Dang, L., Doran, G., Fisher, B., Frankenberg, C., Fu, D., Granat, R., Hobbs, J., Lee, R. A. M., Mandrake, L., McDuffie, J., Miller, C. E., Myers, V., Natraj, V., O'Brien, D., Osterman, G. B., Oyafuso, F., Payne, V. H., Pollock, H. R., Polonsky, I., Roehl, C. M., Rosenberg, R., Schwandner, F., Smyth, M., Tang, V., Taylor, T. E., To, C., Wunch, D., and Yoshimizu, J.: The Orbiting Carbon Observatory-2: first 18 months of science data products, Atmospheric Measurement Techniques, 10, 549–563, https://doi.org/10.5194/amt-10-549-2017, https://www.atmos-meas-tech.net/10/549/2017/, 2017.

Feist, D. G., Arnold, S. G., John, N., and Geibel, M. C.: TCCON data from Ascension Island (SH), Release GGG2014R0, TCCON data archive, hosted by CaltechDATA, https://doi.org/10.14291/tccon.ggg2014.ascension01.R0/1149285, https://tccondata.org, 2014.

Feng, L., Palmer, P. I., Bösch, H., and Dance, S.: Estimating surface CO_2 fluxes from space-borne CO_2 dry air mole fraction observations using an ensemble Kalman Filter, Atmospheric Chemistry and Physics, 9, 2619–2633, https://doi.org/10.5194/acp-9-2619-2009, https://www.atmos-chem-phys.net/9/2619/2009/, 2009.

Geibel, M. C., Messerschmidt, J., Gerbig, C., Blumenstock, T., Chen, H., Hase, F., Kolle, O., Lavrič, J. V., Notholt, J., Palm, M., Rettinger, M., Schmidt, M., Sussmann, R., Warneke, T., and Feist, D. G.: Calibration of column-averaged CH_4 over European TCCON FTS sites with airborne in-situ measurements, Atmospheric Chemistry and Physics, 12, 8763–8775, https://doi.org/10.5194/acp-12-8763-2012, https://www.atmos-chem-phys.net/12/8763/2012/, 2012.

Goo, T.-Y., Oh, Y.-S., and Velazco, V. A.: TCCON data from Anmeyondo (KR), Release GGG2014R0, TCCON data archive, hosted by CaltechDATA, https://doi.org/10.14291/tccon.ggg2014.anmeyondo01.R0/1149284, https://tccondata.org, 2014.

Griffith, D. W., Deutscher, N. M., Velazco, V. A., Wennberg, P. O., Yavin, Y., Aleks, G. K., Washenfelder, R. a., Toon, G. C., Blavier, J.-F., Murphy, C., Jones, N., Kettlewell, G., Connor, B. J., Macatangay, R., Roehl, C., Ryczek, M., Glowacki, J., Culgan, T., and Bryant, G.: TCCON data from Darwin (AU), Release GGG2014R0, TCCON data archive, hosted by CaltechDATA, https://doi.org/10.14291/tccon.ggg2014.darwin01.R0/1149290, https://tccondata.org, 2014a.

Griffith, D. W., Velazco, V. A., Deutscher, N. M., Murphy, C., Jones, N., Wilson, S., Macatangay, R., Kettlewell, G., Buchholz, R. R., and Riggenbach, M.: TCCON data from Wollongong (AU), Release GGG2014R0, TCCON data archive, hosted by CaltechDATA, https://doi.org/10.14291/tccon.ggg2014.wollongong01.R0/1149291, https://tccondata.org, 2014b.

Haring, R., Pollock, R., Sutin, B. M., and Crisp, D.: The Orbiting Carbon Observatory instrument optical design, Proc.SPIE, 5523, 5523 – 5523 – 12, https://doi.org/10.1117/12.562693, https://doi.org/10.1117/12.562693, 2004.

Hase, F., Blumenstock, T., Dohe, S., Gross, J., and Kiel, M.: TCCON data from Karlsruhe (DE), Release GGG2014R1, TCCON data archive, hosted by CaltechDATA, https://doi.org/10.14291/tccon.ggg2014.karlsruhe01.R1/1182416, https://tccondata.org, 2014.

Heymann, J., Reuter, M., Buchwitz, M., Schneising, O., Bovensmann, H., Burrows, J. P., Massart, S., Kaiser, J. W., and Crisp, D.: CO_2 emission of Indonesian fires in 2015 estimated from satellite-derived atmospheric CO_2 concentrations, Geophysical Research Letters, 44, 1537–1544, https://doi.org/10.1002/2016GL072042, https://agupubs.onlinelibrary.wiley.com/doi/abs/10.1002/2016GL072042, 2017.

Iraci, L. T., Podolske, J., Hillyard, P. W., Roehl, C., Wennberg, P. O., Blavier, J.-F., Allen, N., Wunch, D., Osterman, G. B., and Albertson, R.: TCCON data from Edwards (US), Release GGG2014R1, TCCON data archive, hosted by CaltechDATA, https://doi.org/10.14291/tccon.ggg2014.edwards01.R1/1255068, https://tccondata.org, 2016.

Kawakami, S., Ohyama, H., Arai, K., Okumura, H., Taura, C., Fukamachi, T., and Sakashita, M.: TCCON data from Saga (JP), Release GGG2014R0, TCCON data archive, hosted by CaltechDATA, https://doi.org/10.14291/tccon.ggg2014.saga01.R0/1149283, https://tccondata.org, 2014.

Kivi, R., Heikkinen, P., and Kyrö, E.: TCCON data from Sodankyla (FI), Release GGG2014R0, TCCON data archive, hosted by CaltechDATA, https://doi.org/10.14291/tccon.ggg2014.sodankyla01.R0/1149280, https://tccondata.org, 2014.

Liu, J., W. Bowman, K., S. Schimel, D., C. Parazoo, N., Jiang, Z., Lee, M., Bloom, A., Wunch, D., Frankenberg, C., Sun, Y., O'Dell, C., Gurney, K., Menemenlis, D., Gierach, M., Crisp, D., and Eldering, A.: Contrasting carbon cycle responses of the tropical continents to the 2015-2016 El Niño, Science, 358, eaam5690, 2017.

Lucchesi, R.: File Specification for GEOS-5 FP-IT (Forward Processing for Instrument Teams), Tech. rep., NASA Goddard Spaceflight Center, Greenbelt, MD, USA, https://ntrs.nasa.gov/archive/nasa/casi.ntrs.nasa.gov/20150001438.pdf, 2013.

Mandrake, L., O'Dell, C. W., Wunch, D., Wennberg, P. O., Fisher, B., Osterman, G. B., and Eldering, A.: Orbiting Carbon Observatory-2 (OCO-2) Warn Level, Bias Correction, and Lite File Product Description, Tech. rep., Jet Propulsion Laboratory, California Institute of Technology, Pasadena, CA, http://disc.sci.gsfc.nasa.gov/OCO-2/documentation/oco-2-v7/OCO2_XCO2_Lite_Files_and_Bias_Correction_0915_sm.pdf, 2015.

Messerschmidt, J., Macatangay, R., Notholt, J., Petri, C., Warneke, T., and Weinzierl, C.: Side by side measurements of CO_2 by ground-based Fourier transform spectrometry (FTS), Tellus B, 62, 749–758, https://doi.org/10.1111/j.1600-0889.2010.00491.x, https://onlinelibrary.wiley.com/doi/abs/10.1111/j.1600-0889.2010.00491.x, 2010.

Morino, I., Matsuzaki, T., and Shishime, A.: TCCON data from Tsukuba (JP), 125HR, Release GGG2014R1, TCCON data archive, hosted by CaltechDATA, https://doi.org/10.14291/tccon.ggg2014.tsukuba02.R1/1241486, https://tccondata.org, 2014a.

Morino, I., Yokozeki, N., Matzuzaki, T., and Horikawa, M.: TCCON data from Rikubetsu (JP), Release GGG2014R1, TCCON data archive, hosted by CaltechDATA, https://doi.org/10.14291/tccon.ggg2014.rikubetsu01.R1/1242265, https://tccondata.org, 2014b.

Nassar, R., Hill, T. G., McLinden, C. A., Wunch, D., Jones, D. B. A., and Crisp, D.: Quantifying CO_2 Emissions From Individual Power Plants From Space, Geophysical Research Letters, 44, 10,045–10,053, https://doi.org/10.1002/2017GL074702, https://agupubs.onlinelibrary.wiley.com/doi/abs/10.1002/2017GL074702, 2017.

NOAA: National Oceanic and Atmospheric Administration - Where is the highest tide?, https://oceanservice.noaa.gov/facts/highesttide.html, last access: Aug. 2018.

Notholt, J., Petri, C., Warneke, T., Deutscher, N. M., Buschmann, M., Weinzierl, C., Macatangay, R., and Grupe, P.: TCCON data from Bremen (DE), Release GGG2014R0, TCCON data archive, hosted by CaltechDATA, https://doi.org/10.14291/tccon.ggg2014.bremen01.R0/1149275, https://tccondata.org, 2014.

Notholt, J., Warneke, T., Petri, C., Deutscher, N. M., Weinzierl, C., Palm, M., and Buschmann, M.: TCCON data from Ny Ålesund, Spitsbergen (NO), Release GGG2014.R0, TCCON data archive, hosted by CaltechDATA, https://doi.org/10.14291/tccon.ggg2014.nyalesund01.R0/1149278, https://tccondata.org, 2017.

O'Dell, C. W., Connor, B., Bösch, H., O'Brien, D., Frankenberg, C., Castano, R., Christi, M., Eldering, D., Fisher, B., Gunson, M., McDuffie, J., Miller, C. E., Natraj, V., Oyafuso, F., Polonsky, I., Smyth, M., Taylor, T., Toon, G. C., Wennberg, P. O., and Wunch, D.: The ACOS CO_2 retrieval algorithm - Part I: Description and validation against synthetic observations, Atmospheric Measurement Techniques, 5, 99–121, https://doi.org/10.5194/amt-5-99-2012, https://www.atmos-meas-tech.net/5/99/2012/, 2012.

O'Dell, C. W., Eldering, A., Wennberg, P. O., Crisp, D., Gunson, M. R., Fisher, B., Frankenberg, C., Kiel, M., Lindqvist, H., Mandrake, L., Merrelli, A., Natraj, V., Nelson, R. R., Osterman, G. B., Payne, V. H., Taylor, T. R., Wunch, D., Drouin, B. J., Oyafuso, F., Chang, A., McDuffie, J., Smyth, M., Baker, D. F., Basu, S., Chevallier, F., Crowell, S. M. R., Feng, L., Palmer, P. I., Dubey, M., García, O. E., Griffith, D. W. T., Hase, F., Iraci, L. T., Kivi, R., Morino, I., Notholt, J., Ohyama, H., Petri, C., Roehl, C. M., Sha, M. K., Strong, K., Sussmann, R., Te, Y., Uchino, O., and Velazco, V. A.: Improved Retrievals of Carbon Dioxide from the Orbiting Carbon Observatory-2 with the version 8 ACOS algorithm, Atmospheric Measurement Techniques Discussions, 2018, 1–57, https://doi.org/10.5194/amt-2018-257, https://www.atmos-meas-tech-discuss.net/amt-2018-257/, 2018.

Peters, W., Jacobson, A. R., Sweeney, C., Andrews, A. E., Conway, T. J., Masarie, K., Miller, J. B., Bruhwiler, L. M. P., Pétron, G., Hirsch, A. I., Worthy, D. E. J., van der Werf, G. R., Randerson, J. T., Wennberg, P. O., Krol, M. C., and Tans, P. P.: An atmospheric perspective on North American carbon dioxide exchange: CarbonTracker, Proceedings of the National Academy of Sciences, 104, 18 925–18 930, https://doi.org/10.1073/pnas.0708986104, http://www.pnas.org/content/104/48/18925, 2007.

Pollard, D. F., Sherlock, V., Robinson, J., Deutscher, N. M., Connor, B., and Shiona, H.: The Total Carbon Column Observing Network site description for Lauder, New Zealand, Earth System Science Data, 9, 977–992, https://doi.org/10.5194/essd-9-977-2017, https://www.earth-syst-sci-data.net/9/977/2017/, 2017.

Rödenbeck, C.: Estimating CO2 sources and sinks from atmospheric mixing ratio measurements using a global inversion of atmospheric transport, Tech. rep., Max Planck Institute for Biogeochemistry, Jena, Germany, 2005.

Sherlock, V., Connor, B. J., Robinson, J., Shiona, H., Smale, D., and Pollard, D.: TCCON data from Lauder (NZ), 125HR, Release GGG2014R0, TCCON data archive, hosted by CaltechDATA, https://doi.org/10.14291/tccon.ggg2014.lauder02.R0/1149298, https://tccondata.org, 2014.

Strong, K., Mendonca, J., Weaver, D., Fogal, P., Drummond, J., Batchelor, R., and Lindenmaier, R.: TCCON data from Eureka (CA), Release GGG2014R1, TCCON data archive, hosted by CaltechDATA, https://doi.org/10.14291/tccon.ggg2014.eureka01.R1/1325515, https://tccondata.org, 2017.

Suarez, M. J., Rienecker, M. M., Todling, R., Bacmeister, J., Takacs, L., Liu, H. C., Gu, W., S. M., Koster, R. D., and Gelaro, R.: The GEOS-5 Data Assimilation System-Documentation of Versions 5.0.1, 5.1.0, and 5.2.0, Tech. rep., NASA Goddard Spaceflight Center, Greenbelt, MD, USA, https://ntrs.nasa.gov/archive/nasa/casi.ntrs.nasa.gov/20120011955.pdf, 2008.

Sussmann, R. and Rettinger, M.: TCCON data from Garmisch (DE), Release GGG2014R0, TCCON data archive, hosted by CaltechDATA, https://doi.org/10.14291/tccon.ggg2014.garmisch01.R0/1149299, https://tccondata.org, 2014.

Taylor, T. E., O'Dell, C. W., Frankenberg, C., Partain, P. T., Cronk, H. Q., Savtchenko, A., Nelson, R. R., Rosenthal, E. J., Chang, A. Y., Fisher, B., Osterman, G. B., Pollock, R. H., Crisp, D., Eldering, A., and Gunson, M. R.: Orbiting Carbon Observatory-2 (OCO-2) cloud screening algorithms: validation against collocated MODIS and CALIOP data, Atmospheric Measurement Techniques, 9, 973–989, https://doi.org/10.5194/amt-9-973-2016, https://www.atmos-meas-tech.net/9/973/2016/, 2016.

Te, Y., Jeseck, P., and Janssen, C.: TCCON data from Paris (FR), Release GGG2014R0, TCCON data archive, hosted by CaltechDATA, https://doi.org/10.14291/tccon.ggg2014.paris01.R0/1149279, https://tccondata.org, 2014.

Velazco, V. A., Morino, I., Uchino, O., Hori, A., Kiel, M., Bukosa, B., Deutscher, N. M., Sakai, T., Nagai, T., Bagtasa, G., Izumi, T., Yoshida, Y., and Griffith, D. W. T.: TCCON Philippines: First Measurement Results, Satellite Data and Model Comparisons in Southeast Asia, Remote Sensing, 9, https://doi.org/10.3390/rs9121228, http://www.mdpi.com/2072-4292/9/12/1228, 2017.

Warneke, T., Messerschmidt, J., Notholt, J., Weinzierl, C., Deutscher, N. M., Petri, C., Grupe, P., Vuillemin, C., Truong, F., Schmidt, M., Ramonet, M., and Parmentier, E.: TCCON data from Orléans (FR), Release GGG2014R0, TCCON data archive, hosted by CaltechDATA, https://doi.org/10.14291/tccon.ggg2014.orleans01.R0/1149276, https://tccondata.org, 2014.

Wennberg, P. O., Roehl, C., Wunch, D., Toon, G. C., Blavier, J.-F., Washenfelder, R. a., Keppel-Aleks, G., Allen, N., and Ayers, J.: TCCON data from Park Falls (US), Release GGG2014R0, TCCON data archive, hosted by CaltechDATA, https://doi.org/10.14291/tccon.ggg2014.parkfalls01.R0/1149161, https://tccondata.org, 2014a.

Wennberg, P. O., Wunch, D., Roehl, C., Blavier, J.-F., Toon, G. C., and Allen, N.: TCCON data from Caltech (US), Release GGG2014R1, TCCON data archive, hosted by CaltechDATA, https://doi.org/10.14291/tccon.ggg2014.pasadena01.R1/1182415, https://tccondata.org, 2014b.

Wennberg, P. O., Wunch, D., Roehl, C., Blavier, J.-F., Toon, G. C., Allen, N., Dowell, P., Teske, K., Martin, C., and Martin., J.: TCCON data from Lamont (US), Release GGG2014R1, TCCON data archive, hosted by CaltechDATA, https://doi.org/10.14291/tccon.ggg2014.lamont01.R1/1255070, https://tccondata.org, 2016.

Wu, L., Hasekamp, O., Hu, H., Landgraf, J., Butz, A., aan de Brugh, J., Aben, I., Pollard, D. F., Griffith, D. W. T., Feist, D. G., Koshelev, D., Hase, F., Toon, G. C., Ohyama, H., Morino, I., Notholt, J., Shiomi, K., Iraci, L., Schneider, M., de Mazière, M., Sussmann, R., Kivi, R., Warneke, T., Goo, T.-Y., and Té, Y.: Carbon dioxide retrieval from OCO-2 satellite observations using the RemoTeC algorithm and validation with TCCON measurements, Atmospheric Measurement Techniques, 11, 3111–3130, https://doi.org/10.5194/amt-11-3111-2018, https://www.atmos-meas-tech.net/11/3111/2018/, 2018.

Wunch, D., Toon, G. C., Wennberg, P. O., Wofsy, S. C., Stephens, B. B., Fischer, M. L., Uchino, O., Abshire, J. B., Bernath, P., Biraud, S. C., Blavier, J.-F. L., Boone, C., Bowman, K. P., Browell, E. V., Campos, T., Connor, B. J., Daube, B. C., Deutscher, N. M., Diao, M., Elkins, J. W., Gerbig, C., Gottlieb, E., Griffith, D. W. T., Hurst, D. F., Jiménez, R., Keppel-Aleks, G., Kort, E. A., Macatangay, R., Machida, T., Matsueda, H., Moore, F., Morino, I., Park, S., Robinson, J., Roehl, C. M., Sawa, Y., Sherlock, V., Sweeney, C., Tanaka, T., and Zondlo, M. A.: Calibration of the Total Carbon Column Observing Network using aircraft profile data, Atmospheric Measurement Techniques, 3, 1351–1362, https://doi.org/10.5194/amt-3-1351-2010, https://www.atmos-meas-tech.net/3/1351/2010/, 2010.

Wunch, D., Toon, G. C., Blavier, J.-F. L., Washenfelder, R. A., Notholt, J., Connor, B. J., Griffith, D. W. T., Sherlock, V., and Wennberg, P. O.: The Total Carbon Column Observing Network, Philosophical Transactions of the Royal Society of London A: Mathematical, Physical and Engineering Sciences, 369, 2087–2112, https://doi.org/10.1098/rsta.2010.0240, http://rsta.royalsocietypublishing.org/content/369/1943/2087, 2011a.

Wunch, D., Wennberg, P. O., Toon, G. C., Connor, B. J., Fisher, B., Osterman, G. B., Frankenberg, C., Mandrake, L., O'Dell, C., Ahonen, P., Biraud, S. C., Castano, R., Cressie, N., Crisp, D., Deutscher, N. M., Eldering, A., Fisher, M. L., Griffith, D. W. T., Gunson, M., Heikkinen, P., Keppel-Aleks, G., Kyrö, E., Lindenmaier, R., Macatangay, R., Mendonca, J., Messerschmidt, J., Miller, C. E., Morino, I., Notholt, J., Oyafuso, F. A., Rettinger, M., Robinson, J., Roehl, C. M., Salawitch, R. J., Sherlock, V., Strong, K., Sussmann, R., Tanaka, T., Thompson, D. R., Uchino, O., Warneke, T., and Wofsy, S. C.: A method for evaluating bias in global measurements of CO_2 total columns from space, Atmospheric Chemistry and Physics, 11, 12 317–12 337, https://doi.org/10.5194/acp-11-12317-2011, https://www.atmos-chem-phys.net/11/12317/2011/, 2011b.

Wunch, D., Mendonca, J., Colebatch, O., Allen, N., Blavier, J.-F. L., Roche, S., Hedelius, J. K., Neufeld, G., Springett, S., Worthy, D. E. J., Kessler, R., and Strong, K.: TCCON data from East Trout Lake (CA), Release GGG2014R1, TCCON data archive, hosted by CaltechDATA, https://doi.org/10.14291/tccon.ggg2014.easttroutlake01.R1, https://tccondata.org, 2017a.

Wunch, D., Wennberg, P. O., Osterman, G., Fisher, B., Naylor, B., Roehl, C. M., O'Dell, C., Mandrake, L., Viatte, C., Kiel, M., Griffith, D. W. T., Deutscher, N. M., Velazco, V. A., Notholt, J., Warneke, T., Petri, C., De Maziere, M., Sha, M. K., Sussmann, R., Rettinger, M., Pollard, D., Robinson, J., Morino, I., Uchino, O., Hase, F., Blumenstock, T., Feist, D. G., Arnold, S. G., Strong, K., Mendonca, J., Kivi, R., Heikkinen, P., Iraci, L., Podolske, J., Hillyard, P. W., Kawakami, S., Dubey, M. K., Parker, H. A., Sepulveda, E., García, O. E., Te, Y., Jeseck, P., Gunson, M. R., Crisp, D., and Eldering, A.: Comparisons of the Orbiting Carbon Observatory-2 (OCO-2) $X_{\mathrm{CO_2}}$ measurements with TCCON, Atmospheric Measurement Techniques, 10, 2209–2238, https://doi.org/10.5194/amt-10-2209-2017, https://www.atmos-meas-tech.net/10/2209/2017/, 2017b.

Yang, Z., Wennberg, P., Cageao, R., Pongetti, T., Toon, G., and Sander, S.: Ground-based photon path measurements from solar absorption spectra of the O2 A-band, Journal of Quantitative Spectroscopy and Radiative Transfer, 90, 309–321, 2005.

York, D., Evensen, N. M., Martínez, M. L., and De Basabe Delgado, J.: Unified equations for the slope, intercept, and standard errors of the best straight line, American Journal of Physics, 72, 367–375, https://doi.org/10.1119/1.1632486, https://doi.org/10.1119/1.1632486, 2004.

Table 1. OCO-2 v9 instrument-to-spacecraft pointing offsets for each spectral band along the y-axis and z-axis relative to the central boresight of the telescope in units of arcsec.

		FP1	FP2	FP3	FP4	FP5	FP6	FP7	FP8
y-axis	O2 A-band	1339.5	972.4	597.2	225.0	-140.6	-508.1	-879.6	-1241.6
	weak CO2 band	1331.0	966.2	604.7	235.9	-131.5	-499.4	-860.8	-1226.4
	strong CO2 band	1359.1	987.3	614.7	244.0	-125.9	-496.0	-867.1	-1242.7
z-axis	O2 A-band	-96.4	-109.0	-117.8	-122.8	-124.1	-121.6	-115.3	-105.2
	weak CO2 band	-58.0	-62.9	-65.7	-66.4	-65.0	-61.4	-55.7	-47.9
	strong CO2 band	-55.2	-57.9	-58.4	-56.6	-52.6	-46.4	-37.9	-27.2

Table 2. Overview of the truth proxy training data sets for v9.

Name	N_s land $\left(\times 10^3\right)$	N_s ocean glint $\left(\times 10^3\right)$	date	Details
TCCON	614	360	Sep. 2014 - May 2018	GGG2014 (see Tab. 6)
Multi-Model Median	956	2691	Sep. 2014 - March 2017	Median of 9 models
SAA	63	287	Sep. 2014 - Jan. 2017	areas <100 km along-track

Table 3. Models that contribute to the Multi-Model Median truth proxy data set.

Name/Group	Version	Land/Biosphere	Inverse Method	Transport	Reference
CAMS	15r2	ORCHIDEE	4D-Var	LMDZ	Chevallier et al. (2010)
CarbonTracker	CT2015,CT-NRT.v2016-1	CASA	EnKF	TM5	Peters et al. (2007)
TM5-4DVar-NOAA	2016	SiB-CASA	4D-Var	TM5	Basu et al. (2013)
OU	2016	CASA	4D-Var	TM5	Crowell et al. (2018)
Baker		CASA-GFEDv3	4D-Var	PCTM	Baker et al. (2010)
CMS-Flux		CASA-GFEDv3	4D-Var	GEOS-CHEM	Liu et al. (2017)
CSU-1		SiB4/MERRA	Bayesian Synthesis	GEOS-CHEM	
Jena CarboScope	s04_v3.8	Special	4D-Var	TM3	Rödenbeck (2005)
Univ. Edinburgh	v2.1	CASA	EnKF	GEOS-CHEM	Feng et al. (2009)

Table 4. Parametric bias correction coefficients and reference values for v9 over land and ocean.

land nadir/glint	$\mathrm{dP_{frac}}$	co2_grad_del	DWS
coefficients	-0.900	-0.029	-9.000
reference values	0.0	15.0	0.0
ocean glint	$\mathrm{dP_{sCO_2}}$	max(co2_grad_del, -6)	
coefficients	-0.245	0.090	
reference values	0.0	-6.0	

Table 5. Filter variables and limits for the X_{CO_2} quality flag definition in v9.

variable	meaning	land filter	ocean filter
co2_ratio	Ratio of Band 2 to Band 3 CO_2 column from IDP algorithm	[1.00, 1.023]	[1.00, 1.02]
h2o_ratio	Ratio of Band 2 to Band 3 H_2O column from IDP algorithm	[0.88, 1.01]	[0.88, 1.01]
dP_{O_2}	Retrieved minus prior surface pressure [hPa]	[-8, 11]	[-5, 9]
dP_{sCO_2}	Retrieved minus prior surface pressure [hPa]	[-10, 12]	[-5, 9]
dP_{ABP}	Retrieved minus prior surface pressure from ABP algorithm [hPa]	[-12, 16]	[-50, 10]
windspeed	Retrieved surface wind speed [m/s]		[1.5, 25]
co2_grad_del	Retrieved vertical gradient in CO_2 [ppm]	[-60, 85]	[-18, 30]
Altitude Stddev	Standard deviation of the surface elevation in the FOV [m]	[0, 110]	
Band 3 albedo	Retrieved albedo strong CO_2 band	[0.03, 0.6]	
albedo_slope_wco2	Retrieved slope of the Lambertian component of the surface albedo using the strong CO_2 band $\left[\mathrm{cm}^{-1}\right]$		[-1.5, 1.2]·1e-5
albedo_slope_sco2	Retrieved slope of the Lambertian component of the surface albedo using the strong CO_2 band $\left[\mathrm{cm}^{-1}\right]$	[-13, 100]·1e-5	[0.6, 7]*1e-5
rms_rel_wco2	Relative RMS of Band 2 fit residuals [%]	[0, 0.28]	[0, 0.3]
rms_rel_sco2	Relative RMS of Band 3 fit residuals [%]	[0, 0.45]	
τ_{total}	Retrieved optical depth of all aerosol types	[0, 0.5]	
τ_{WA}	Retrieved optical depth of water cloud	[0.0005, 0.1]	
τ_{IC}	Retrieved optical depth of ice cloud	[0.00, 0.04]	[0, 0.035]
τ_{ST}	Retrieved optical depth of stratospheric aerosol	[0.0002, 0.02]	
τ_{OC}	Retrieved optical depth of organic carbon	[0, 0.2]	
τ_{SS}	Retrieved optical depth of sea salt	[0, 0.125]	
H_{IC}	Retrieved relative pressure height of ice cloud	[-0.5, 0.5]	
DWS	Retrieved optical depth of three large aerosol types (dust, water cloud, and sea salt)	[0, 0.25]	
eof33rel	Retrieved relative amplitude of third EOF of Band 3		[-0.3, 0.25]
$\chi^2_{\mathrm{wCO_2}}$	Reduced χ^2 value of the L2FP fit residuals for Band 2		[0, 2]
$X_{CO_2,\mathrm{uncert.}}$	Posterior uncertainty in X_{CO_2} [ppm]		[0.28, 1.10]
Max_Declocking_wco2	See O'Dell et al. (2018) for details		[0, 0.27]
Max_Declocking_sco2	See O'Dell et al. (2018) for details		[0, 0.34]

Table 6. Stations used in the TCCON truth proxy data set

TCCON station	Reference	TCCON station	Reference
Anmyeondo, South Korea	Goo et al. (2014)	Lamont, OK, USA	Wennberg et al. (2016)
Ascension Island	Feist et al. (2014)	Lauder, New Zealand	Sherlock et al. (2014)
Bialystok, Poland	Deutscher et al. (2014)	Manaus, Brazil	Dubey et al. (2014)
Burgos, Phillipines	Velazco et al. (2017)	Ny Ålesund, Spitzbergen, Norway	Notholt et al. (2017)
Bremen, Germany	Notholt et al. (2014)	Orléans, France	Warneke et al. (2014)
Caltech, Pasadena, CA, USA	Wennberg et al. (2014b)	Paris, France	Te et al. (2014) (2014)
Darwin, Australia	Griffith et al. (2014a)	Park Falls, WI, USA	Wennberg et al. (2014a)
Edwards (Armstrong), CA, USA	Iraci et al. (2016)	Réunion Island	De Mazière et al. (2014)
East Trout Lake, Canada	Wunch et al. (2017a)	Rikubetsu, Japan	Morino et al. (2014b)
Eureka, Canada	Strong et al. (2017)	Saga, Japan	Kawakami et al. (2014)
Garmisch, Germany	Sussmann and Rettinger (2014)	Sodankylä, Finland	Kivi et al. (2014)
Izaña, Tenerife, Spain	Blumenstock et al. (2014)	Tsukuba, Japan	Morino et al. (2014a)
Karlsruhe, Germany	Hase et al. (2014)	Wollongong, Australia	Griffith et al. (2014b)

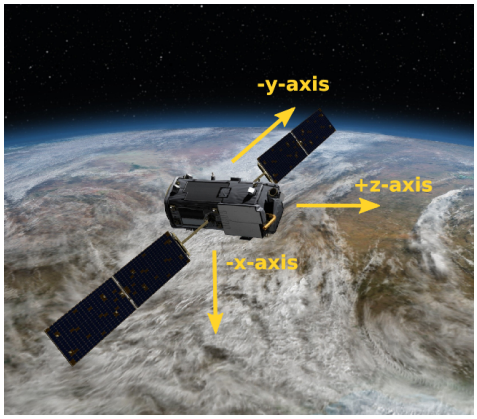

Figure 1. Illustration of the OCO-2 spacecraft body axes.

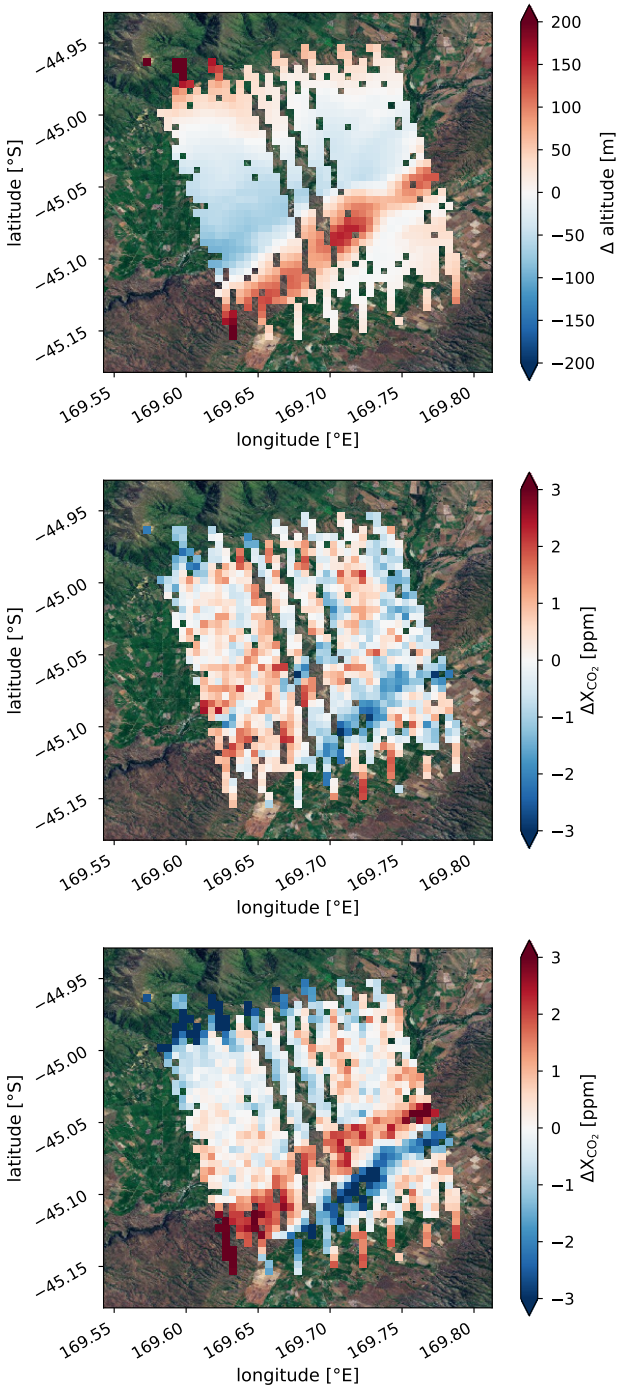

Figure 2. OCO-2 target mode observation over Lauder, New Zealand on February 17, 2015. The upper panel shows Δ altitude (defined as the sounding altitude minus the median altitude of all soundings in the given latitude and longitude limits). The middle and lower panel show the variation of raw and bias-corrected OCO-2 v8 ΔX_{CO_2} (defined in the same way as Δ altitude) after applying the v8 filters. Individual soundings are aggregated into $0.005^\circ \times 0.005^\circ$ latitude-longitude square grids.

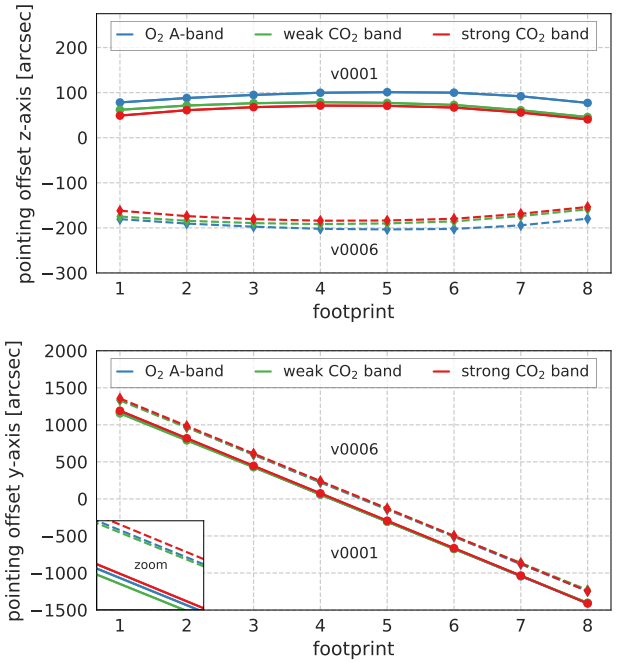

Figure 3. OCO-2 pointing offsets for each footprint and spectral band for the z-axis (upper panel) and y-axis (lower panel) derived from the pre-launch (v0001) and on-orbit (v0006) analyses.

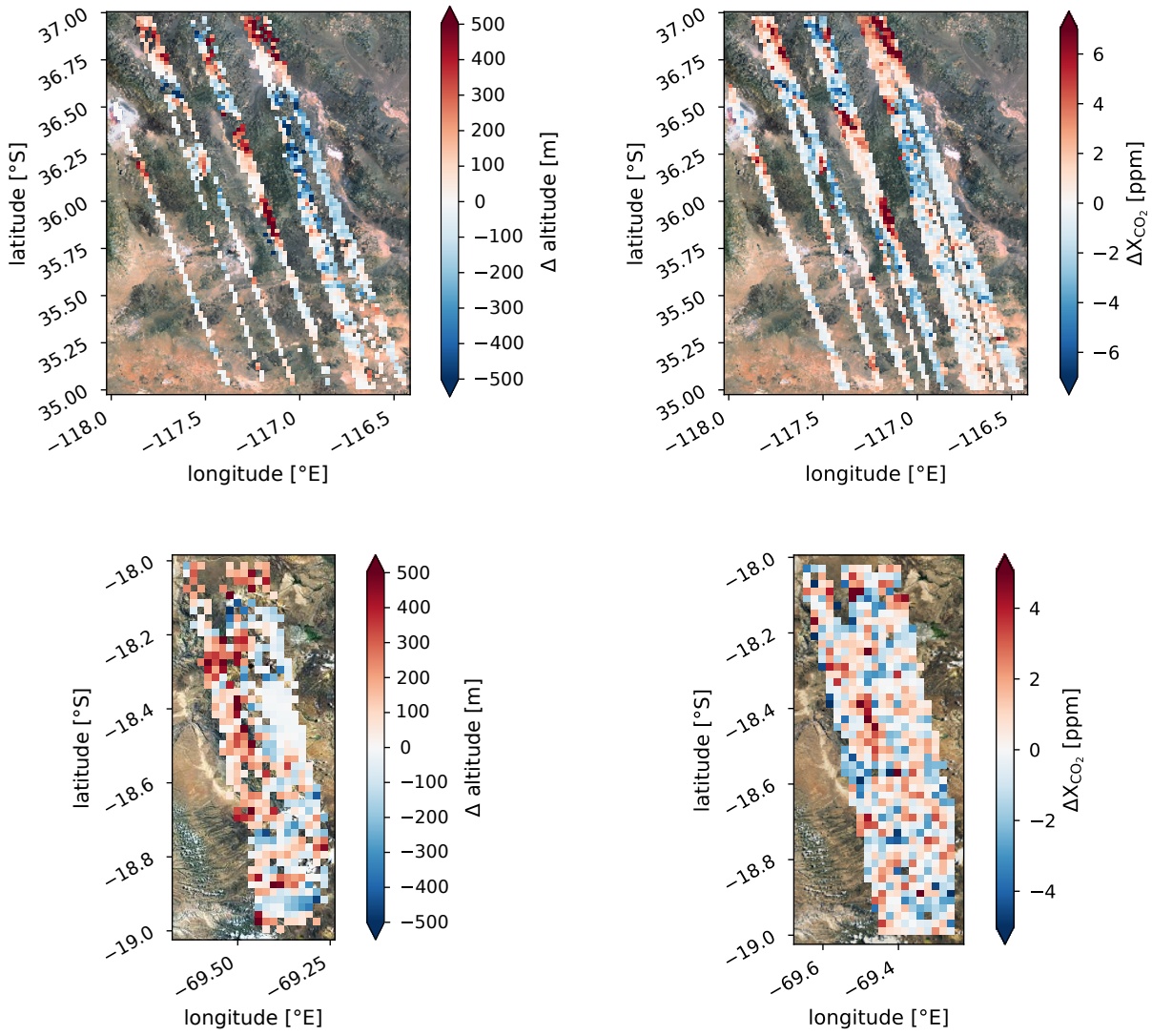

Figure 4. Change in altitude (left column) over the two selected areas in the Death Valley National Park (upper row) and Atacama Desert (lower row). The change in altitude is determined from two $0.02^\circ \times 0.02^\circ$ latitude-longitude grid squares in the NE direction in the Northern Hemisphere and the SE direction in the Southern Hemisphere, hence the figures have fewer values than for ΔX_{CO_2} (right column). Steep topography with total altitude changes of up to 1000 m are observed in both areas. A topography related bias in ΔX_{CO_2} derived from the ACOS L2FP retrieval is apparent in both regions. Individual observations are aggregated into $0.02^\circ \times 0.02^\circ$ latitude-longitude grid squares.

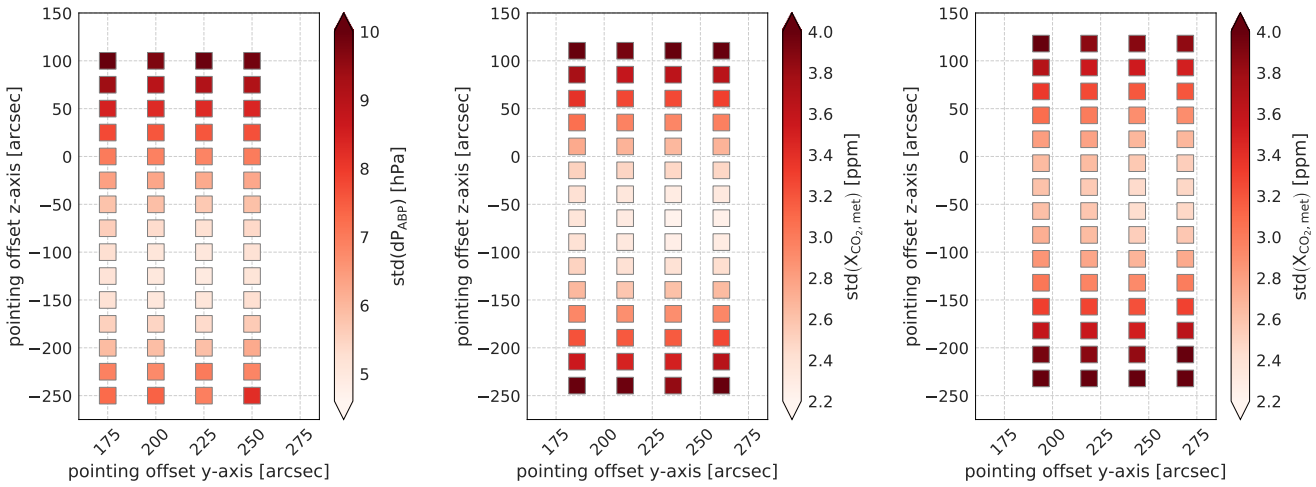

Figure 5. Standard deviation of $\mathrm{dP_{ABP}}$ (left panel) and $\mathrm{X_{CO_{2,met}}}$ for the weak (middle panel) and strong (right panel) CO_2 band for FP4 for all 60 geolocation configurations for the Death Valley National Park.

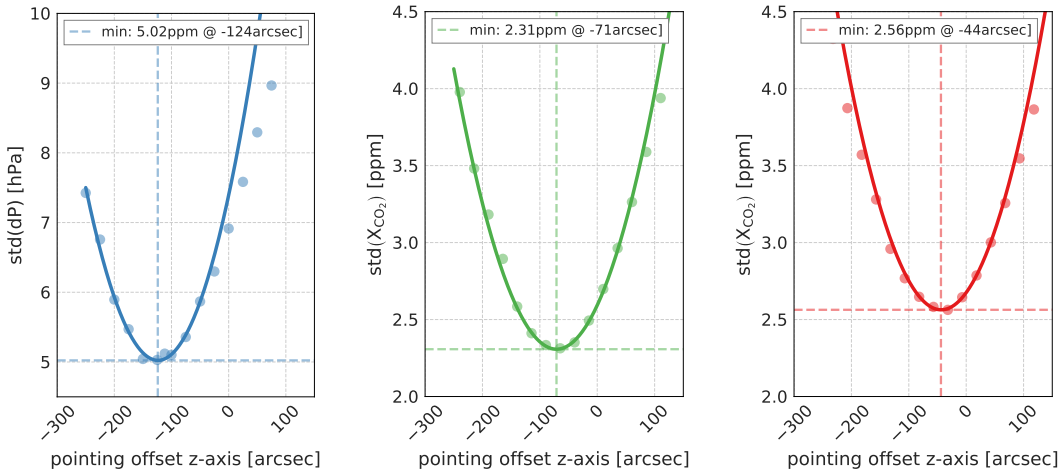

Figure 6. Standard deviation of $\mathrm{dP_{ABP}}$ (left panel) and $\mathrm{X_{CO_{2,met}}}$ of the weak (middle panel) and strong (right panel) CO_2 bands as a function of z-axis pointing offsets for FP4 for the Death Valley National Park. To determine the minimum, only values that are distributed symmetrically around the minimum are taken into account for the quadratic regression.

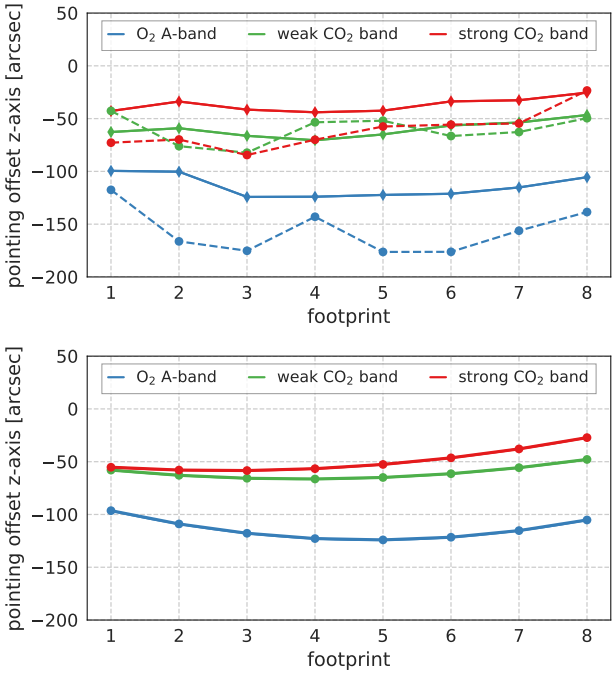

Figure 7. Upper panel: z-axis footprint pointing offsets for the three spectral bands for the Death Valley National Park (solid) and Atacama Desert (dashed); lower panel: z-axis footprint pointing offsets used in the OCO-2 v9 geometric calibration algorithm.

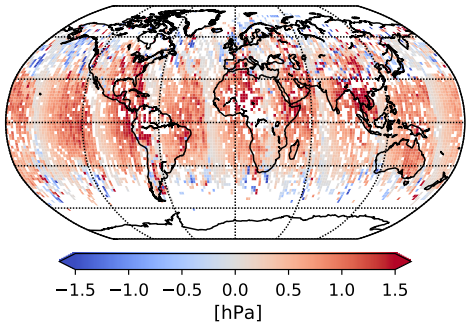

Figure 8. Mean difference between v9 and v8 (v9 - v8) surface pressure prior for April 2016. Data is aggregated into $2^\circ \times 2^\circ$ latitude-longitude square grids.

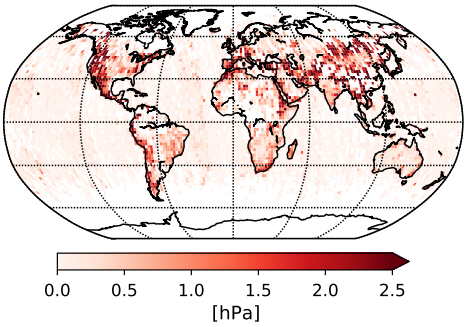

Figure 9. Difference between v9 and v8 (v9 - v8) of the surface pressure prior standard deviation in each grid cell for April 2016. Data is aggregated into $2^\circ \times 2^\circ$ latitude-longitude square grids.

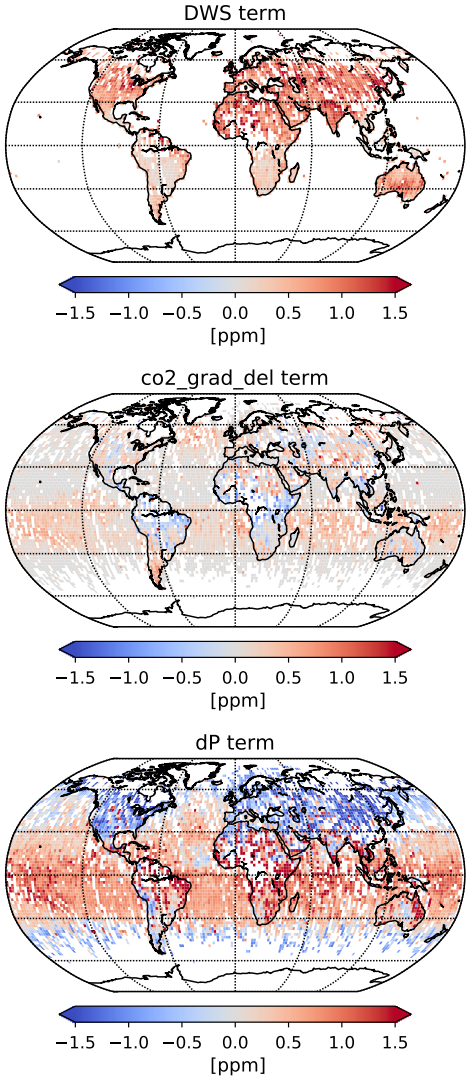

Figure 10. Contributions of the parametric bias correction terms to raw X_{CO_2} from DWS (upper panel, only over land), co2_grad_del (middle panel), and the two dP terms over land and ocean (lower panel) for April 2016. Data is aggregated into $2^\circ \times 2^\circ$ latitude-longitude square grids.

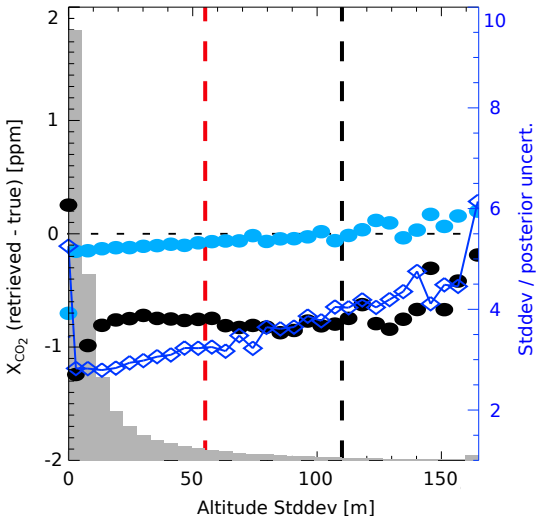

Figure 11. Difference between v9 $\mathrm{X_{CO_2}}$ and the Multi-Model Median data set over land (nadir and glint) as a function of the standard deviation of the surface elevation in the FOV given in m. Shown are the mean bias, aggregated into 10 m bins, for both raw (black circles) and bias-corrected (light blue circles) $\mathrm{X_{CO_2}}$. The standard deviation of the bias-corrected $\mathrm{X_{CO_2}}$ difference is marked by dark blue diamonds. The distribution of the standard deviation of the surface elevation for the time period Sept. 2014 - March 2017 is shown in gray. The vertical black dashed line represents the v9 upper filter limit. The vertical red line represents the upper limit used in v8.

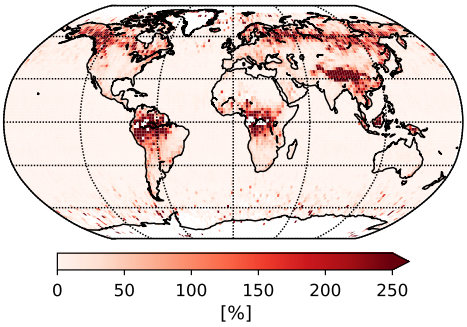

Figure 12. Relative increase of soundings that pass the v9 filtration scheme compared to v8 for the entire year 2016. Data is aggregated into $2^\circ \times 2^\circ$ latitude-longitude square grids.

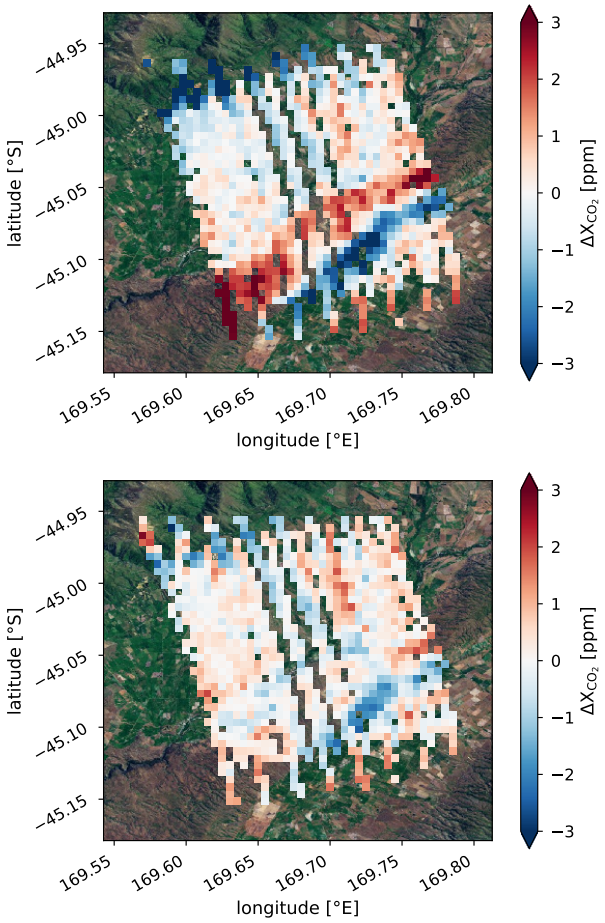

Figure 13. v8 (upper panel) and v9 (lower panel) bias corrected $\mathrm{X}_{\mathrm{CO}_2}$ over Lauder, New Zealand on February 17, 2015. $\Delta\mathrm{X}_{\mathrm{CO}_2}$ is defined in the same way as in Fig. 2. Data is aggregated into $0.005^\circ \times 0.005^\circ$ latitude-longitude square grids.

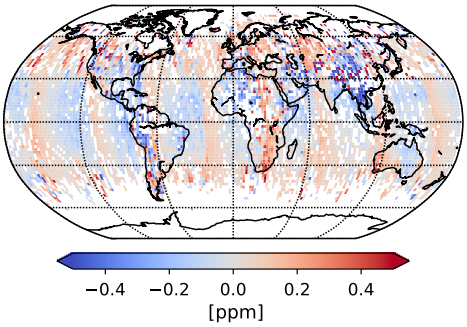

Figure 14. Global difference between v8 and v9 (v9 - v8) bias corrected X_{CO_2} for April 2016. Only soundings that passed the v8 and v9 filtration are taken into account. A mean bias of 0.15 ppm (mainly introduced by the different global scaling factors for v8 and v9) is subtracted. Data is aggregated into $2^\circ \times 2^\circ$ latitude-longitude square grids.

Appendix A: Theoretical motivation of dP parameters in the v9 parametric bias correction

Column-averaged dry-air mole fractions of CO_2 are defined as the total column of CO_2 (C_{CO_2}) divided by the dry air column (C_{dryair}):

$$\mathrm{X_{CO_2}} = \frac{C_{CO_2}}{C_{\mathrm{dryair}}} \tag{A1}$$

C_{dryair} is defined as:

$$C_{\mathrm{dryair}} = \frac{\mathrm{P}}{g_0 \cdot m_{\mathrm{dryair}}} - \frac{C_{\mathrm{H_2O}} \cdot m_{\mathrm{H_2O}}}{m_{\mathrm{dryair}}} \tag{A2}$$

Here, P is the surface pressure, g_0 the gravitational acceleration, $C_{\mathrm{H_2O}}$ the total column of water vapour, m_{dryair} the mean molecular weight of dry air, and $m_{\mathrm{H_2O}}$ the mean molecular weight of water vapor. The surface pressure P can be written as:

$$\mathrm{P} = c \cdot \mathrm{P_{ap}} + (1-c) \cdot \mathrm{P_{ret}} \tag{A3}$$

$\mathrm{P_{ap}}$ and $\mathrm{P_{ret}}$ represent the prior and retrieved surface pressure, respectively. The parameter c is the fractional weight given to the prior in the assumed surface pressure. A value of $c = 0$ means that we completely trust the retrieval, $c = 1$ means that we completely trust the prior. For a start, we neglect the contribution of the total column of water vapor. Then the dry air column is directly proportional to the surface pressure and we can write:

$$\mathrm{X_{CO_2,raw}} \propto \frac{C_{\mathrm{CO_2}}}{\mathrm{P_{ret}}} \tag{A4}$$

For bias-corrected $\mathrm{X_{CO_2}}$ we can write:

$$\mathrm{X_{CO_2,bc}} \propto \frac{C_{\mathrm{CO_2}}}{c \cdot \mathrm{P_{ap}} + (1-c) \cdot \mathrm{P_{ret}}} = \frac{\mathrm{X_{CO_2,raw}} \cdot \mathrm{P_{ret}}}{c \cdot \mathrm{P_{ap}} + (1-c) \cdot \mathrm{P_{ret}}} = \frac{\mathrm{X_{CO_2,raw}}}{c \cdot (\mathrm{P_{ap}}/\mathrm{P_{ret}}) + (1-c)} \tag{A5}$$

Taylor expansion in c around $c = 0$ leads to:

$$\mathrm{X_{CO_2,bc}} = \mathrm{X_{CO_2,raw}} + c \cdot \underbrace{\mathrm{X_{CO_2,raw}} \cdot \left(1 - \frac{\mathrm{P_{ap}}}{\mathrm{P_{ret}}}\right)}_{\mathrm{dP_{frac}}} \tag{A6}$$

The second term in Eq. (A6) is identical to the $\mathrm{dP_{frac}}$ parameter that is used in the v9 parametric bias correction over land (see Sect. 4.1). Here, c represents the coefficient for the dP parameter in the parametric bias correction over land. If we assume that relative variations in $\mathrm{X_{CO_2,raw}}/\mathrm{P_{ret}}$ are small compared to relative variations in $(\mathrm{P_{ret}} - \mathrm{P_{ap}})$, then we can further simplify to:

$$\mathrm{X_{CO_2,bc}} = \mathrm{X_{CO_2,raw}} + c \cdot (\mathrm{P_{ret}} - \mathrm{P_{ap}}) \tag{A7}$$

The second term of Eq. (A7) has the form of the $\mathrm{dP_{sCO_2}}$ parameter as defined in Sect. 4.1. This form, however, does not account for the fractional change in $\mathrm{X_{CO_2}}$ at higher elevations when error is present in surface pressure estimates. Therefore, we use Eq. (A6) over land and Eq. (A7) only over ocean. Note that the parametric bias correction coefficient c in Eq.(A6) and Eq.(A7) is different for land and ocean observations (see Tab.4).